University of Alberta

Heat Transfer and Calorimetry of Tubular Ni/WC Wires Deposited with GMAW

by

Kevin M. Scott

A thesis submitted to the Faculty of Graduate Studies and Research
in partial fulfillment of the requirements for the degree of

Master of Science

in

Welding Engineering

Department of Chemical and Materials Engineering

Fall 2011
Edmonton, Alberta

Abstract

A calorimeter for the deposition of metal during free-flight GMAW was developed for the purpose of measuring droplet heat content in Ni/WC tubular wires. By approximating the thermal gradients within the calorimeter to be second order polynomials the energy transferred to the calorimeter by the droplets was accounted for with more accuracy than previous investigations. Testing with 1.2 mm (0.045 in.) ER70S-6 steel wire agreed with previous studies and confirmed a minimum droplet temperature in the transition between globular and spray transfer.

Arc characteristics of the Ni/WC consumable were unstable and the transition from globular to spray transfer was gradual without a distinct demarkation. For a 1.6 mm (0.0625 in.) tubular wire manufactured by H.C. Starck droplet heat content reached a minimum at approximately 190 A using a voltage setting of 26.9 V, 172 in/min wire feed speed, 12.5 mm (0.5 in.) electrode extension and 12.5 mm arc length. Subsequent bead-on-plate trials indicated increased carbide survival at the minimum droplet heat content compared with a similar overlay at non-optimum parameters. Small, polygonal secondary carbides were nucleated indicating dissolution and re-precipitation occurred even at the optimum parameters.

Acknowledgements

It was an early August day back in 2008; I had just arrived back in Golden from a summer internship in New York the previous day and was helping my colleagues in the foundry clean up before the beginning of the Fall semester. Patricio happened to come down to the lab to check on our progress, and mentioned to me that he would like to speak with me in his office before the day was through. Little did I know that our conversation in his office would mark the beginning of the next chapter in my life.

Edmonton, Alberta is an industrial town; a far cry from the beauty of the foothills that I lived day in and day out during my residency at Mines. But, looking back, the past two years have been the most important in my life. Patricio was not only a one-of-a-kind advisor, he was a friend, counselor and mentor. Patricio has a unique perspective of both science and the world that is very unique and insightful, and I am forever indebted to him for having the opportunity to get to know him and his family. Patricio, thank you for the meaningful discussions, the numerous laughs and even a couple tears.

I would like to thank Syncrude and NSERC for their financial contributions to this project, and also the numerous sponsors of the Canadian Centre for Welding and Joining, in particular Bruce Albrecht and Rick Hutchison of Miller Electric Mfg. Co. for the donation of the welding equipment and Mike Ho at JV Driver for the table on which the apparatus was built.

There is no possible way I would have made it through the past two years without the help of Terry Runyon. Not only did she have an answer for every question I had, but knew someone to call or even took care of the issue herself. Terry is a remarkable person, and I am thankful to have had the opportunity to work with her.

Thank you to Walter Boddez, Les Dean and Richard Cooper in the instrument shop for their assistance with data acquisition, and to Gentry Wood, Brett Burger and Stuart Guest for their contribution to this work. Thanks also to Matt Dewar for help with Thermocalc.

Thank you is not enough for my wife, Janine. You were beyond supportive of my decision to head up to Alberta, dealt with living in the city and through it all baked me more brownies and cakes than I could have wished for.

To Nikoli, whom this thesis is dedicated, thank you for teaching me what is truly valuable.

Contents

List of Figures

List of Tables

Chapter 1 : Introduction

The oil sands in Northern Alberta represent one of the largest hydrocarbon deposits in the world [1] containing valuable, recoverable oil that can help fuel North America and the world for years to come. Averaging 1.49 million barrels per day in 2009, the rate of production is expected to double by 2019 [2]. While much of these reserves are recoverable by in-situ operations, a significant portion must be recovered using non-traditional techniques. In these techniques the sand is excavated and the oil removed through a series of upgrading steps. The excavation of the oil is taxing on the equipment due to the overly erosive and corrosive nature of the sand/oil mixture. As a result, overlays have been used to help minimize the effects of the sand on the tooling. While several different overlay alloys are used extensively in the mining industry, nickel based, tungsten carbide reinforced (Ni/WC) overlays are ideal for protecting equipment from the oil sands due to their superior wear and corrosion resistant properties [3]. Due to the low heat of formation of tungsten carbide (WC) [3], WC powders dissolve in molten metal when exposed for sufficient time at sufficient temperature.

Plasma Transferred Arc Welding (PTAW), a process in which a non-consumable tungsten electrode establishes an arc between itself and the base material, is the traditional process used for Ni/WC overlay deposition [4, 5]. Ni and WC powders are fed through orifices on either side of the arc, as seen in Figure 1.1.

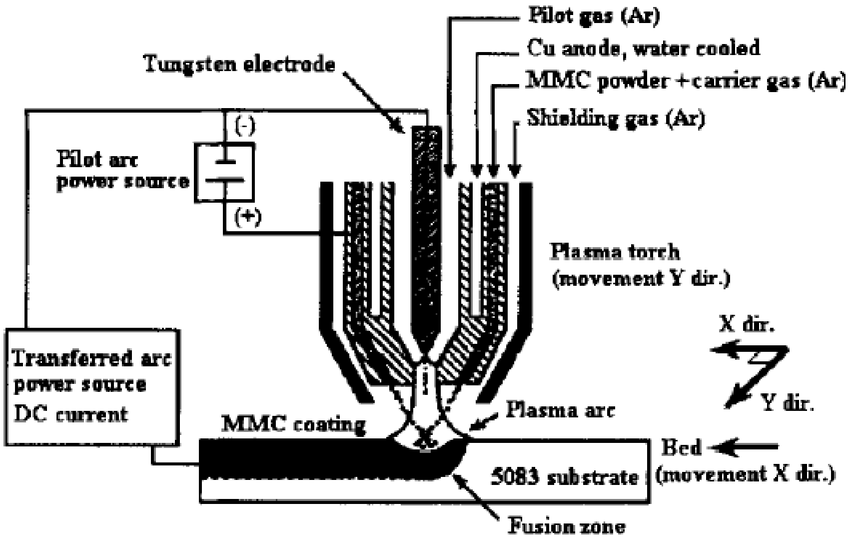

Figure 1.1 Schematic of the PTAW process [4].

This process has several advantages, especially when depositing Ni/WC overlays. The powders are injected near the bottom of the arc so they do not experience severe temperatures. Therefore the likelihood of the WC dissolving in the Ni matrix is very small. Also, the PTAW process is easily automated and results in very high quality, uniform depositions that yield superior wear resistance. The use of powders inherently limits the PTAW process to the vertical position due to the gravity fed powder delivery system. When welding out of position or in the field, PTAW is no longer feasible.

There is a need for a process that produces overlays of comparable quality to PTAW but offers more flexibility to enable field repair and out of position deposition. Gas Metal Arc Welding (GMAW) is a possible alternative. Not only is the process flexible and easy to use, but the cost of equipment is significantly less than that of PTAW. The consumable is delivered in the form of a wire with the powder contained within to make out of position overlays realistic and simple. Field repair with GMAW is feasible because of the flexibility and portability of the welding equipment.

There are fundamental limitations inherent to GMAW, however. In GMAW the nickel sheath and carbide powders are exposed to severe temperature gradients due to the arc establishing between the electrode and base material. Figure 1.2 shows the arc attachment configuration for globular transfer in GMAW.

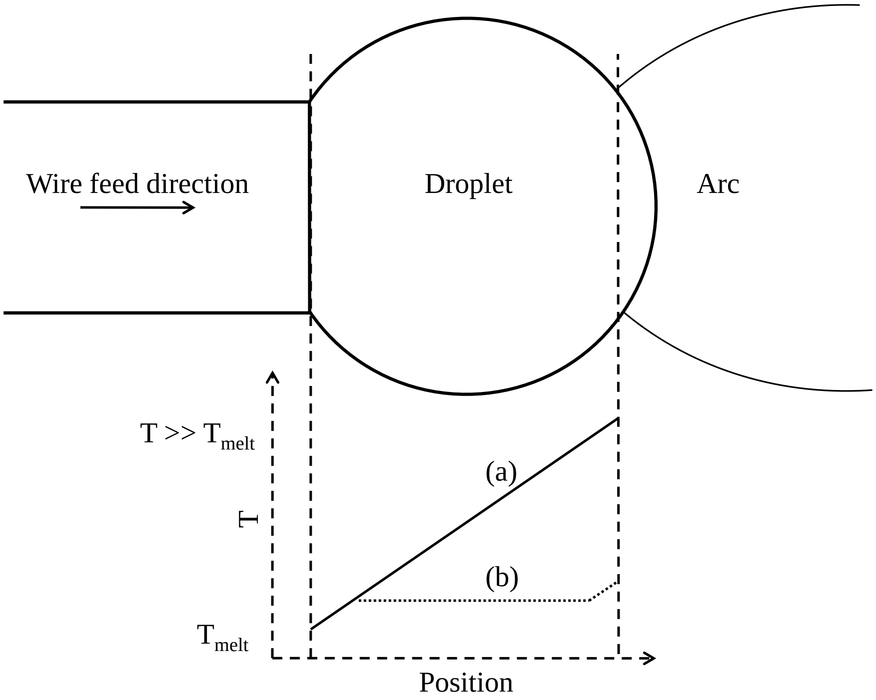

Figure 1.2 Thermal gradient(s) in the droplets in globular transfer. When the gradient establishes, the average temperature of the droplet increases. Note: typical GMAW operation is vertical.

Shown in Figure 1.2 are two distinct thermal gradient conditions. In (a), convective flows within the droplets are nonexistent and energy is transferred from the anode spot to the melting interface by conduction. In (b) convection plays a significant role in heat transfer between the anode spot and melting interface resulting in moderated droplet temperatures [6, 7]. In both cases, the molten droplet is superheated to a temperature above the melting temperature of the electrode material. This condition is non-ideal for Ni/WC deposition because of the dissolution of the carbide into the matrix material [3]. The feasibility of deposition with GMAW has been studied [8-11]; the researchers concluded that although adequate under some conditions, overall carbide dissolution was higher in GMAW deposits than PTAW deposits.

Previous research on solid consumables has predicted [12] and measured [13] a minimum droplet heat content between globular and spray transfer modes. Should this minimum exist in tubular wires, it is possible that it would be substantial enough to minimize carbide dissolution. The emphasis of the current study was calorimetry of free-flight GMAW using Ni/WC tubular consumables to identify and quantify a minimum in droplet heat content. Calorimetry was necessary to account for the average heat content of the entire deposit. Although optical pyrometry [14] and direct thermocouple measurement [15, 16] has been used, the surface temperature of the droplets can be significantly different than the core thus introducing significant uncertainty in the two latter methods.

This study will be limited to one Ni/WC consumable, the H.C. Starck CTC 1.6 mm (0.0625 in.) wire, to minimize variation in the process. This wire was chosen based on successful results obtained in hot-wire Gas Tungsten Arc Welded (GTAW) deposits [17]. Contact tip to work distance (CTWD) and electrode extension (EE) are held constant at 12.5 mm (0.5 in.). The contact point between the electrode and contact tip is controlled using a specially designed contact tip detailed in Appendix A along with the experimental setup.

The following chapter describes the calorimeter designs used in previous work and the design, testing and implementation of the calorimeter used in this study. After, the effective material properties for tubular consumables is introduced followed by implementation of the equations to predict droplet heat content in Ni/WC consumables. The results are then outlined followed by discussion, the conclusions and recommendations for future work. Finally, located within the appendices are the experimental setup, a summary of the effective materials properties, a mechanical drawing of the calorimeter and supporting calculations.

Chapter 2 : Calorimeter Design

The devices used to measure droplet heat content in free-flight GMAW vary greatly, but all rely on the principles of calorimetry. The droplets are collected within a medium, the temperature of which is monitored by thermocouples. Droplet heat content and droplet temperature are calculated based on the temperature change in the calorimeter and thermophysical properties of the filler material being tested. The following sections outline the previous work on calorimetry of GMAW and later describe the design and implementation of the calorimeter used in the current study.

Previous Work on Welding Calorimetery

Beginning in the mid-1960's droplet temperature and heat content became the focus of significant interest to researchers and industry. Workplace cleanliness and worker health were becoming more important as advanced alloys were being developed. To quantify and understand how droplet heat content changes with welding current and transfer mode researchers used the various apparatus described in the following paragraphs.

In two studies, Pokhodnya and Suptel [18, 19] utilized a setup that incorporated several calorimeter systems, shown in Figure 2.1. An arc was established between a 2 mm (0.079 in.) diameter mild or alloy steel electrode and a rotating copper disk. The droplets that detached fell through a copper tube before being collected in the solid-state copper calorimeter. The tube and the calorimeter were thermally isolated from each other to prevent heat transfer, and the influence of the arc plasma was minimized by the use of a screening collar. Immediately after the arc was extinguished the screening collar was plugged with an asbestos cap. The purpose of the copper tube was to capture any radiant heat that was lost as the droplets were in free fall. The temperature of the tube and calorimeter was monitored by two separate thermocouples.

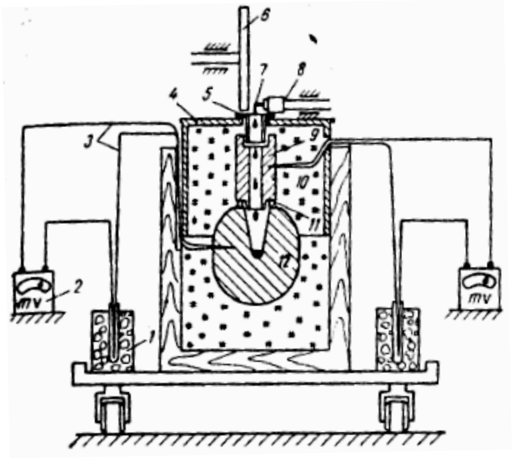

Figure 2.1 Schematic representation of the setup used by Pokhodnya and Suptel [18, 19].

The authors report that while operating in electrode positive (EP) polarity, droplet temperature increases with increased welding current until the enthalpy saturates at a critical limit, the boiling point of the electrode material. While operating in electrode negative (EN) polarity, droplet temperature and welding current are directly related, although the droplet temperature in EN is 300-600 °C lower than while operating in EP. The authors note the erratic nature of the arc while operating in EN, and cite surface oxides and excess lubricant left over from drawing the wire as being conducive to the instability.

Ando and Nishiguchi [20] also explored the heat content of copper and aluminum droplets in GMAW and came to similar conclusions as Pokhodnya and Suptel. The authors found an increase in droplet enthalpy with welding current, and report droplet temperatures approaching the boiling point of the material while operating in the spray transfer region. To measure heat content, the authors used a water bath calorimeter in which the droplets were caught by a copper crucible. The arc was established between a GMAW torch and a Gas Tungsten Arc Welding (GTAW) anode. After detachment, the droplets fell through several heat shields before being collected by the crucible. A schematic of that setup is shown in Figure 2.2.

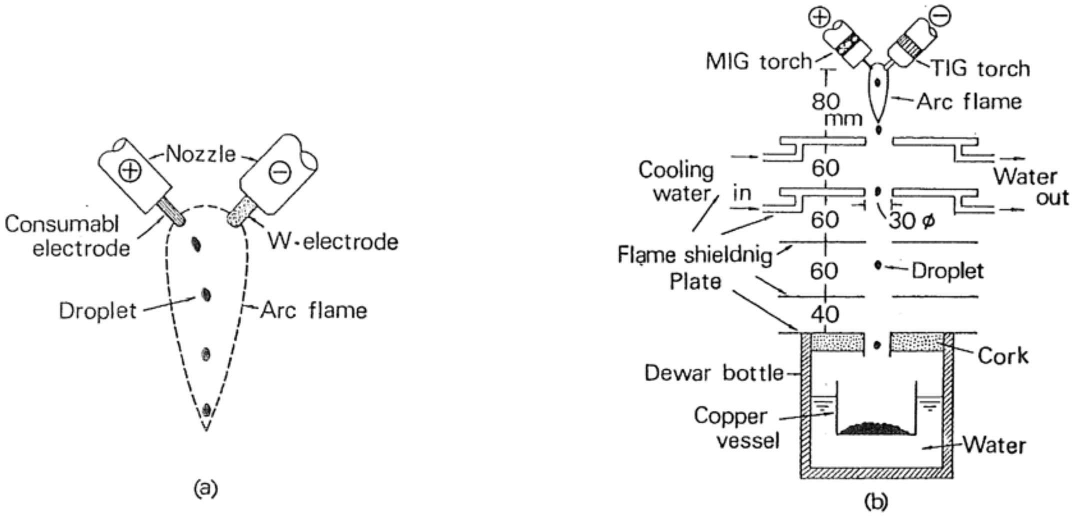

Figure 2.2 Schematic representation of the calorimeter used by Ando and Nishiguchi [20]. The droplet falls 30 cm (11.8 in.) prior to collection.

In this study, arc voltage was held constant while the welding current was changed, resulting in varying electrode extension (EE) and arc lengths. The authors reported that as EE is increased, droplet heat content decreased.

Ozawa and Morita [21] used a calorimeter similar to Ando and Nishiguchi. The arc was established between a plate and a 4 or 2.3 mm (0.16 or 0.09 in.) electrode while the droplets were allowed to fall through an aluminum plate and thermal insulator before being collected in a copper crucible submerged in a water bath, shown in Figure 2.3. Iron, aluminum and copper electrodes are reviewed with results in agreement with other researchers. The researchers noted that as EE is decreased, droplet heat content increased.

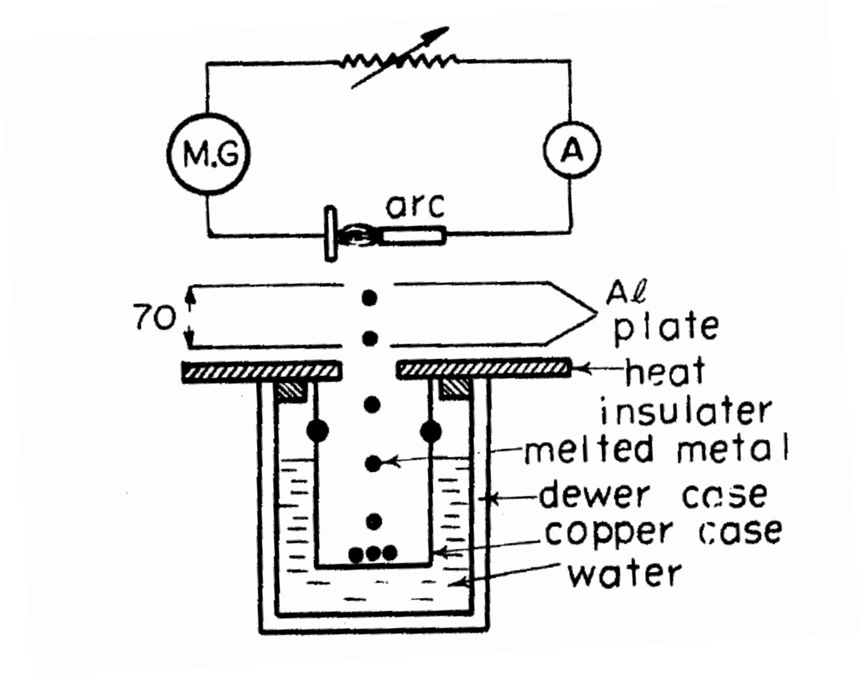

Figure 2.3 Schematic of the calorimeter used by Ozawa and Morita [21]. The droplet falls only 70 mm (2.75 in.) before being encapsulated by the calorimeter.

Heiro and North [22] studied the effects of pulse energy on droplet temperature using a calorimeter very similar to Pokhodnya and Suptel. The main components of the calorimeter were a copper sphere that collected the droplets as well as a copper tube that absorbed radiant energy from the droplets as they fell. The calorimeter was insulated by being placed in a vacuum chamber that was pumped to a pressure of 4 Pa (0.03 mm Hg). The design of the sphere was such that the total temperature increase of the calorimeter was no more than 50 °C when 50 g of material was collected. The total mass of the tube and calorimeter was 7.897 kg (17.4 lb). EE was kept at 12.5 mm (0.5 in.) for all tests, while the contact tip was maintained at 25 mm (1.0 in.) from the top of the calorimeter. The researchers noted that droplet temperature is highly dependent on the pulse energy.

Fu, Ushio and Matsuda [23] utilized a concept similar to those mentioned above, except that the calorimeter was kept in an inert argon atmosphere to prevent the droplets from oxidizing while traveling from the electrode to the calorimeter. The arc was established between the electrode and a carbon plate. The authors studied the effects of shielding gas composition and Joule heating on electrode melting. The authors report that shielding gas composition and arc length have little effect on the melting rate of steel wire.

Lu and Kou [15, 24] used several calorimetric methods to determine droplet heat content, and also utilized two direct measurement methods using tungsten-rhenium thermocouples, a method also used by Jelmorini *et al.* [16]. One calorimeter configuration was similar to the one used by Ando and Nishiguchi, while the other was a novel approach in which a water-cooled copper cathode was used to establish the arc while the droplets fell through to the calorimeter. This method is shown in Figure 2.4, while another method used by Lu and Kou is shown in Figure 2.5

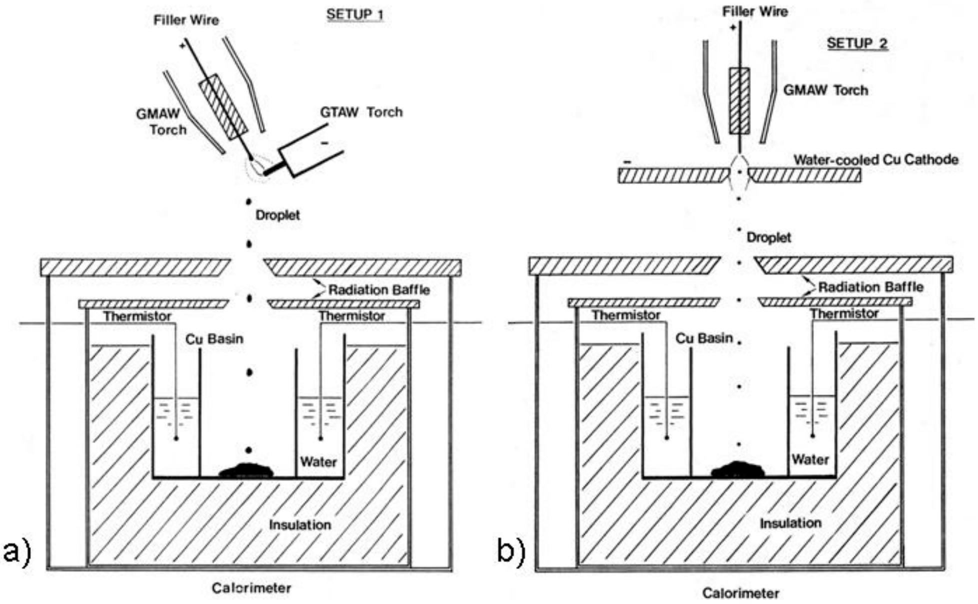

Figure 2.4 Water-cooled copper cathode set-up (right) utilized by Lu and Kou [15] alongside a variation of the setup.

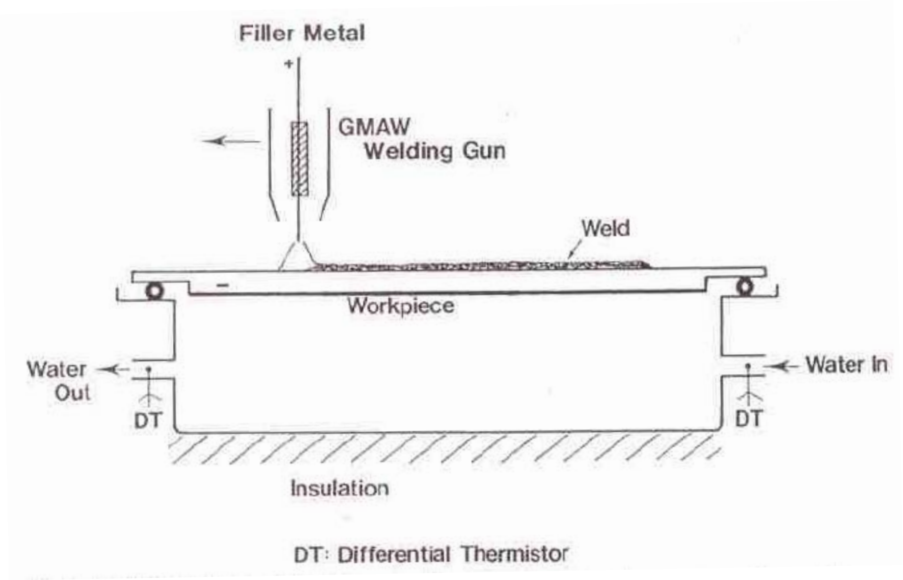

Figure 2.5 Bead-on-plate calorimetry method used by Lu and Kou [24]. This method is a good approximation of the process efficiency in an industrial situation.

With the calorimeter and thermocouple-based experimental setups, Lu and Kou reported and increase in droplet temperature well into the spray transfer mode until the temperature approaches, but does not pass, the boiling point of the material.

Soderstrom [13, 25] used a method similar to Lu and Kou's water-cooled copper cathode setup. Unlike previous researchers, who focused on measuring droplet temperature at relatively distant welding current increments, Soderstrom focused on the area near the transition from globular to spray transfer resulting in much finer current resolution. By doing so, Soderstrom reported a minimum droplet temperature around the transition from globular to spray transfer using solid aluminum, steel and stainless steel wires shielded with pure argon. The results are shown in Figure 2.6. Electrode extension and arc length were kept constant at 12.5 mm (0.5 in.).

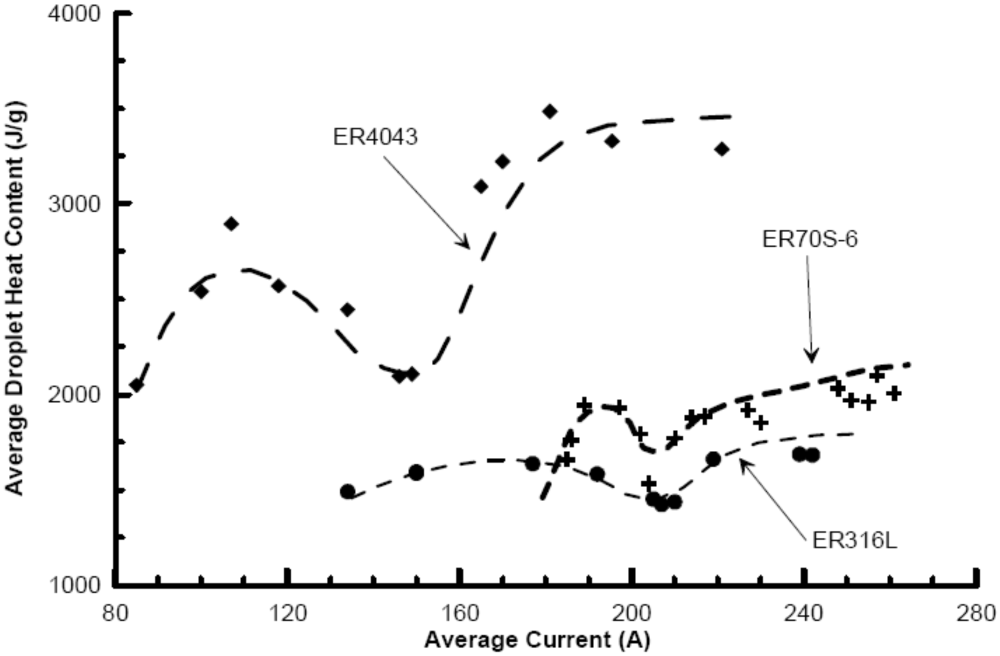

Figure 2.6 Average droplet heat content for ER4043 aluminum, ER70S-6 steel and ER304L stainless steel wires. From [25].

Calorimeter Design Considerations

While water bath calorimeters are effective, this approach is inherently limiting as convection is responsible for heat transfer in the water bath. Some researchers used a mechanical stirring rod to force convection, but doing so establishes thermal and velocity boundary layers that remain unaccounted for. Also, the maximum temperature of the bath is limited to less than 100 °C to avoid energy loss to vaporization. The following section describes the benefits of using a solid state calorimeter as well as the considerations made in the current study. Calibration results and a comparison to previous studies follow.

The solid-state calorimeter used in this study was engineered specifically for the purpose of collecting molten metal droplets and measuring the change of enthalpy of the mass of deposited metal. The main benefit of using a solid state calorimeter is to eliminate the complexities of convective currents that exist with water-bath calorimeters while also eliminating the possibility of heat loss through evaporation. The solid-state calorimeters used in previous research [18, 19, 22] are very large and use only one thermocouple to monitor the temperature change in the calorimeter. This suggests that the authors are assuming uniform temperature throughout the mass; however, it is likely that this is not the case considering the thermal diffusion lengths involved in these calorimeters.

A cylindrical section of 50.8 mm (2 in.) diameter ultra-high purity (99.99%) copper was chosen as the material for the calorimeter. The dimensions of the calorimeter were calculated based on an approximation of the energy change in the calorimeter when a small volume of molten metal was deposited on the surface, shown in Appendix B. Temperature gradients within the mass were estimated using second order polynomials in three dimensions. Approximation of the polynomials in all three directions renders symmetric deposition of metal on the calorimeter a secondary consideration. This is critical for this particular study because the pattern of deposition can be erratic and unpredictable, especially for the tubular wires of interest.

The general enthalpy profile in the copper mass of the calorimeter can be approximated as:

$$H(x,y,z) = \sum_{i=1}^{10} h_i(x,y,z)H_i$$

Equation 2.1

Where H is the volumetric enthalpy (J/m^3), h_i are dimensionless second order polynomials and H_i is the enthalpy measured at each thermocouple position (J/m^3). Fitting a dimensionless second order polynomial in x, y and z leaves the function h_i:

$$h_i(x,y,z) = c_{i,1} + c_{i,2}x + c_{i,3}y + c_{i,4}z + c_{i,5}xy + c_{i,6}xz + c_{i,7}yz + c_{i,8}x^2 + c_{i,9}y^2 + c_{i,10}z^2$$

Equation 2.2

where x, y and z are the rectangular coordinates of each thermocouple, given in Appendix B, and $c_{i,1\text{-}10}$ are calculated for each thermocouple position. The calculation of h_i can be made by using the property that $h_i = 1$ for the location of thermocouple i and $h_j = 0$ for the remaining thermocouple positions $i \neq j$. For example, for thermocouple 1:

$$\begin{bmatrix} 1 & x_1 & y_1 & z_1 & x_1y_1 & x_1z_1 & y_1z_1 & x_1^2 & y_1^2 & z_1^2 \\ 1 & x_2 & y_2 & z_2 & x_2y_2 & x_2z_2 & y_2z_2 & x_2^2 & y_2^2 & z_2^2 \\ 1 & x_3 & y_3 & z_3 & x_3y_3 & x_3z_3 & y_3z_3 & x_3^2 & y_3^2 & z_3^2 \\ 1 & x_4 & y_4 & z_4 & x_4y_4 & x_4z_4 & y_4z_4 & x_4^2 & y_4^2 & z_4^2 \\ 1 & x_5 & y_5 & z_5 & x_5y_5 & x_5z_5 & y_5z_5 & x_5^2 & y_5^2 & z_5^2 \\ 1 & x_6 & y_6 & z_6 & x_6y_6 & x_6z_6 & y_6z_6 & x_6^2 & y_6^2 & z_6^2 \\ 1 & x_7 & y_7 & z_7 & x_7y_7 & x_7z_7 & y_7z_7 & x_7^2 & y_7^2 & z_7^2 \\ 1 & x_8 & y_8 & z_8 & x_8y_8 & x_8z_8 & y_8z_8 & x_8^2 & y_8^2 & z_8^2 \\ 1 & x_9 & y_9 & z_9 & x_9y_9 & x_9z_9 & y_9z_9 & x_9^2 & y_9^2 & z_9^2 \\ 1 & x_{10} & y_{10} & z_{10} & x_{10}y_{10} & x_{10}z_{10} & y_{10}z_{10} & x_{10}^2 & y_{10}^2 & z_{10}^2 \end{bmatrix} \times \begin{bmatrix} c_{1,1} \\ c_{1,2} \\ c_{1,3} \\ c_{1,4} \\ c_{1,5} \\ c_{1,6} \\ c_{1,7} \\ c_{1,8} \\ c_{1,9} \\ c_{1,10} \end{bmatrix} = \begin{bmatrix} 1 \\ 0 \\ 0 \\ 0 \\ 0 \\ 0 \\ 0 \\ 0 \\ 0 \\ 0 \end{bmatrix}$$

Equation 2.3

where $c_{1,1\text{-}10}$ are obtained by inverting the left hand matrix. Equation 2.3 solves for the constants at position 1; the others are calculated in the same manner but setting the h_i function of interest to 1. The overall enthalpy of the body is then given by:

$$H_{tot} = \int_V H \, dV$$

Equation 2.4

Equation 2.4 can be re-written by substituting Equation 2.1:

$$H_{tot} = \int_V \sum_{i=1}^{10} h_i(x, y, z)\, H_i\, dV = \sum_{i=1}^{10} \left[\int_V h_i(x, y, z) dV \right] H_i$$

Equation 2.5

leaving:

$$H_{tot} = \rho_o \sum_{i=1}^{10} v_i H_i$$

Equation 2.6

where H_{tot} is the overall enthalpy of the body in J, ρ_o is the initial density of the cylinder in kg/m^3 and H_i is the mass enthalpy (J/kg) calculated from each thermocouple position. v_i , the integrated form of h_i , has units of m^3 and is represented by:

$$v_i = c_{i,1}V + \frac{2\pi H^2 R^2}{4} c_{i,4} + \frac{\pi H R^4}{4} c_{i,8} + \frac{\pi H R^4}{4} c_{i,9} + \frac{2\pi H^3 R^2}{6} c_{i,10}$$

Equation 2.7

where H, R and V are the height, radius and initial volume of the cylinder respectively. Due to symmetry the constants $c_{i,2}$, $c_{i,3}$ and $c_{i,5\text{-}7}$ all equal zero. This integration is shown in Appendix C. First order theory was used to calculate the overall enthalpy of the calorimeter so subtle volume changes with temperature did not affect calculations. Enthalpy was used in these calculations to eliminate the uncertainty in using the specific heat capacity, c_p, which may vary with temperature. This concept is shown in Figure 2.7. The overall enthalpy change was calculated in Equation 2.13 and was independent of these variances.

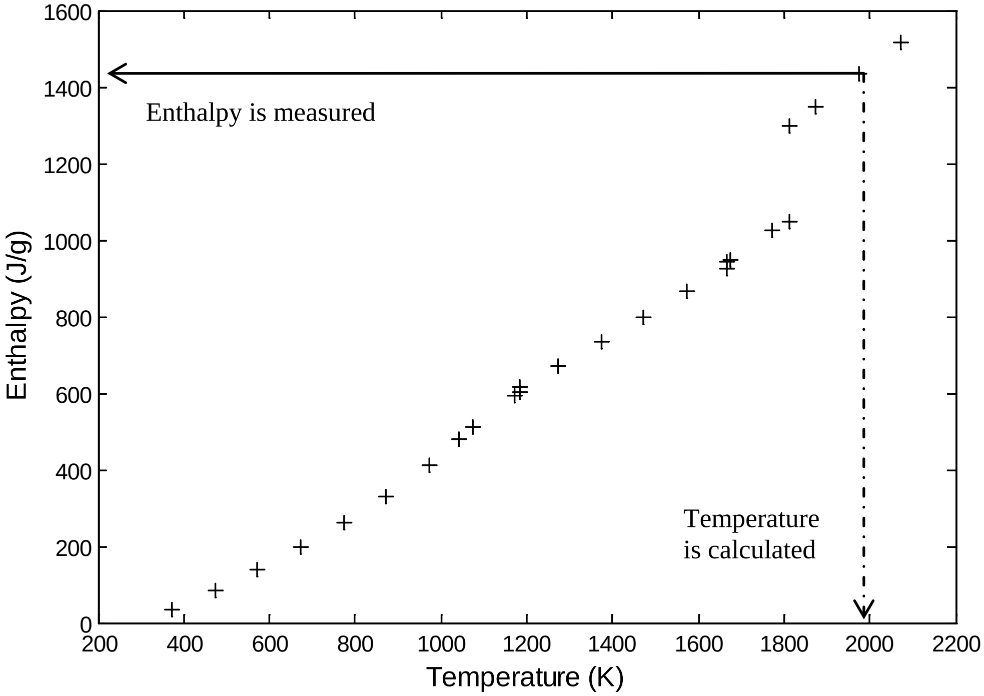

Figure 2.7 Enthalpy response to temperature for pure iron [26]. The arrows indicate the measures value, enthalpy, and how it relates to temperature.

Calorimeter Calibration

Calibration of the calorimeter was completed using liquid tin at a known initial temperature. Tin was chosen as an ideal material for calibration due to its low melting temperature and well tabulated enthalpy data. The tin was melted in a crucible that was insulated on the sides. The bottom surface of the crucible remained exposed so that it could be heated with a propane torch. The setup used for calibration is shown in Figure 2.8. After the tin was completely molten and superheated, the flame used to heat the crucible was turned off and the temperature was allowed to equilibrate. When the temperature in the bath was uniform, a small quantity of tin was deposited onto the calorimeter.

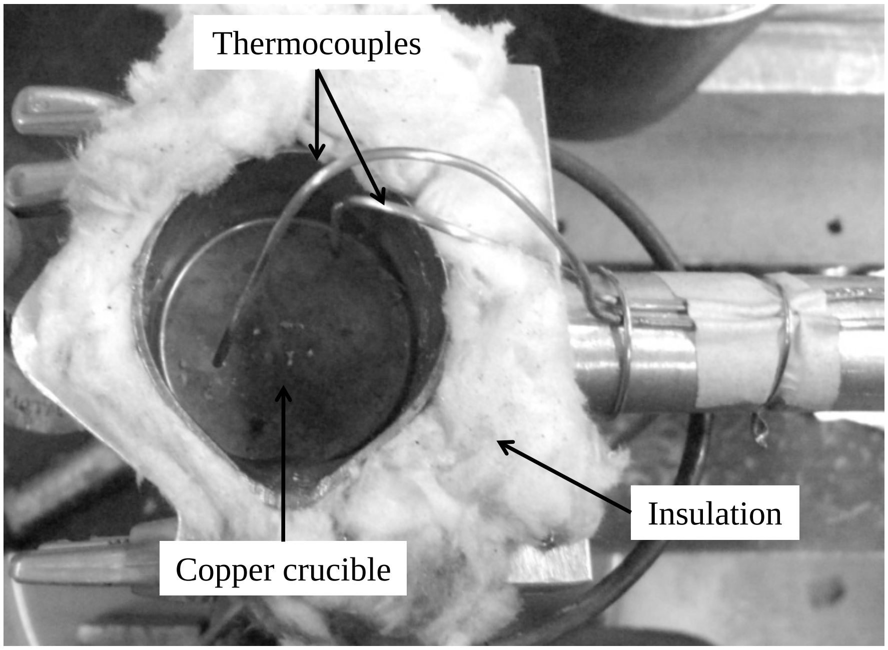

Figure 2.8 Setup used for tin calibration. Temperature was monitored in two places within the molten bath to ensure uniform temperature prior to deposition.

Table D.1 in Appendix D shows the results of the calibration. Theoretically, at room temperature the calorimeter should not gain or lose energy. As the calorimeter temperature begins to rise above the ambient temperature it is reasonable to expect that energy will be dissipated to the surroundings. Figure 2.9 shows the amount of discrepancy between the known energy deposited and the energy measured. Below temperatures of ~350 K (77 °C) the calorimeter measured more energy than was deposited.

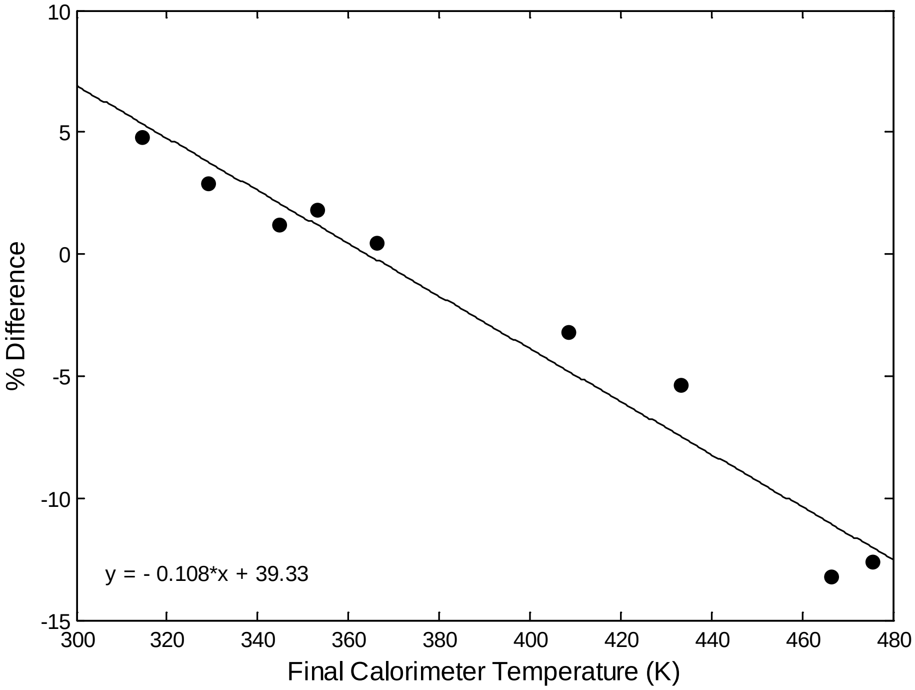

Figure 2.9 Uncertainty in the calorimeter calibration. This example shows systematic uncertainty in the calorimeter setup.

Ultimately the cause for this discrepancy can be one of three places: the thermocouple readings, the tabulated enthalpy data for tin or the tabulated enthalpy data for copper. The thermocouples were calibrated using a Fluke 9173 Metrology Well; therefore, the likelihood of significant uncertainty in the thermocouple readout is minimal. Figure 2.10 shows the tabulated enthalpy data for copper and tin.

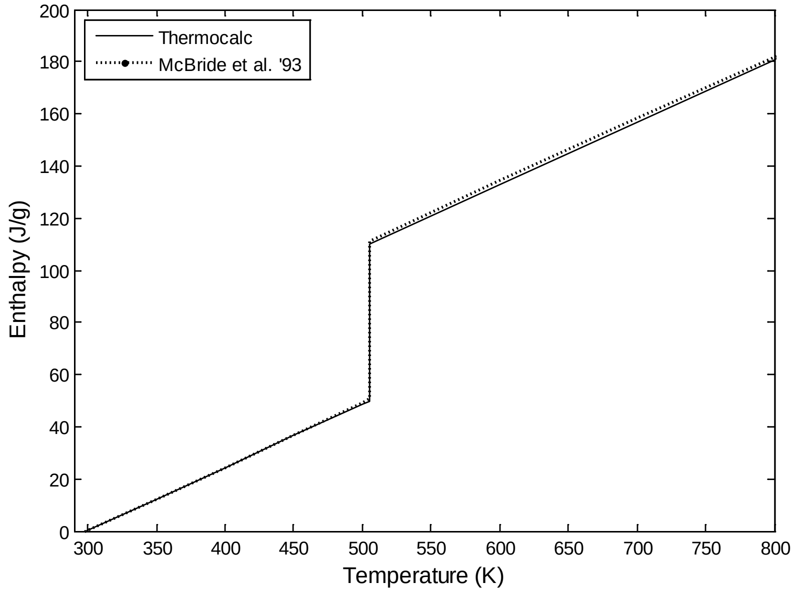

(a)

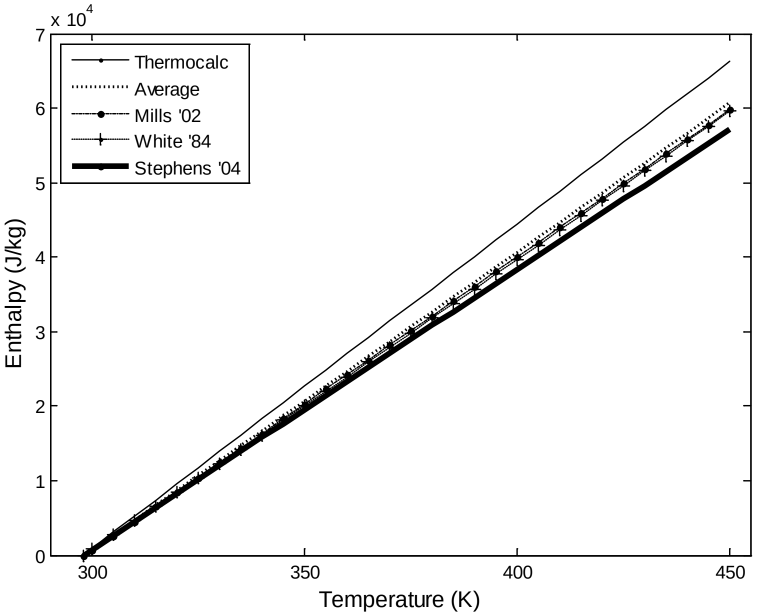

(b)

Figure 2.10 Tabulated enthalpy data for tin (a) and copper (b). The discrepancy between sources for tin is insignificant, however the sources for copper report significantly different values over the temperature range of the calorimeter.

Tin data are taken from Thermocalc Database SSOL4 and McBride *et al.[27]* while copper data were taken from Thermocalc Database SSOL4, Mills [26], White and Collocott [28] and Stephens [29]. There is little uncertainty in the tabulated tin data; however, there is significant discrepancy in the copper data. At the temperatures of interest the tabulated enthalpy values for copper can vary by as much as 15%. Figure 2.11 shows the result of the calibration if each source was used to calculate the calorimeter enthalpy separately along with the average between all sources.

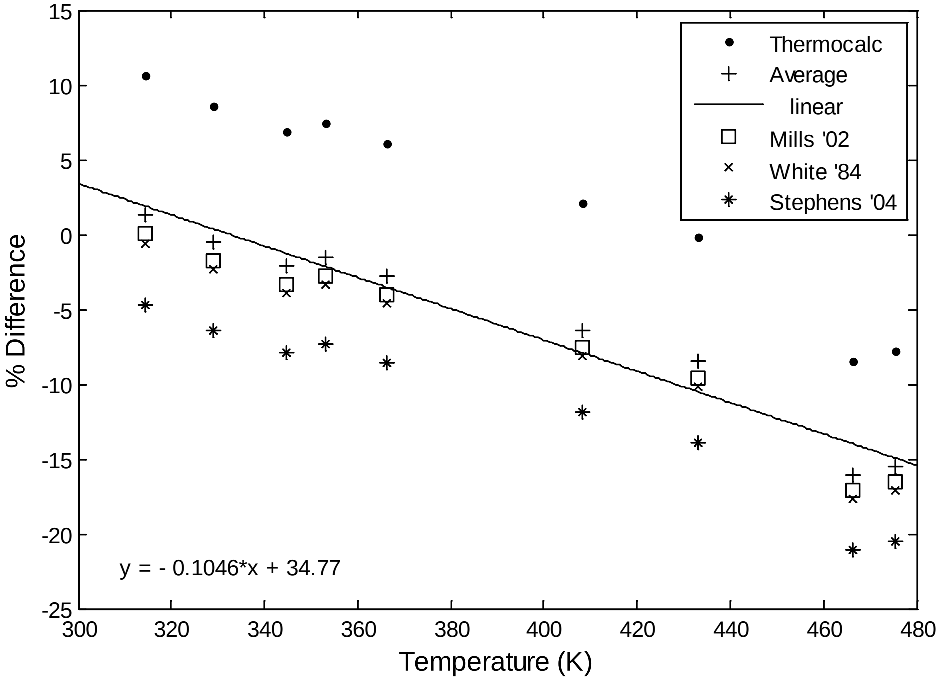

Figure 2.11 Discrepancy plotted against final calorimeter temperature for all copper sources and the average.

In Figure 2.11 a linear regression of the average discrepancy is shown. From Figure 2.11 it is clear that for the regression to room temperature the total enthalpy of the calorimeter is calculated to be more than what was deposited by approximately 3.5%. The intersection of the linear regressions of these data are distributed about 0% difference. For this reason, and the fact that it would match the theoretical behavior, the regression was shifted to pass through 0% difference at room temperature (298 K) and accounted for in a correction function that calibrated the calorimeter. This is shown in Figure 2.12.

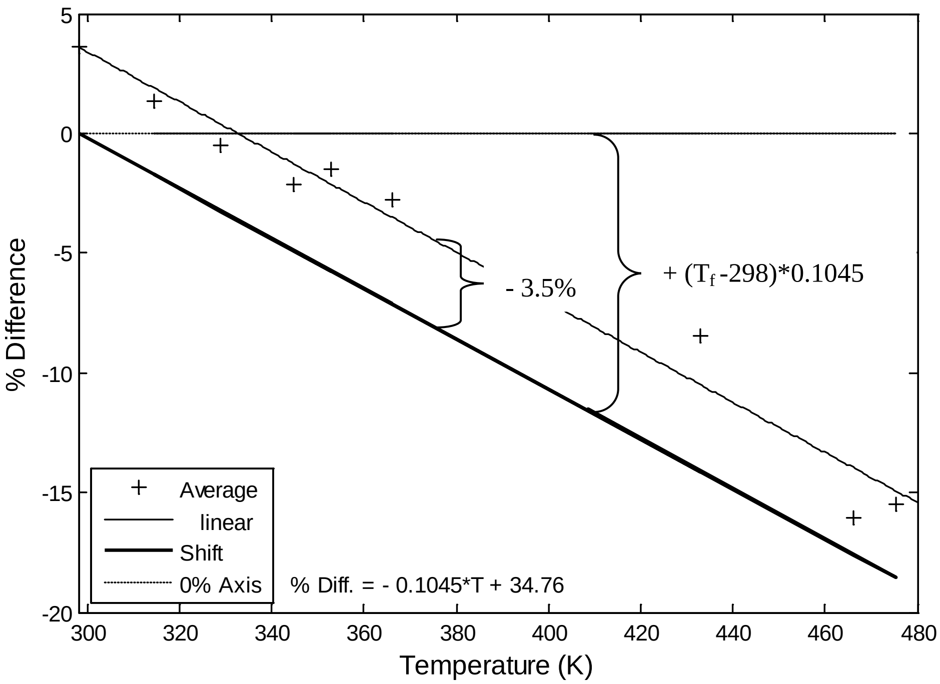

Figure 2.12 Shift of the average discrepancy to pass through 0% at room temperature. The graph shows how energy was subtracted then added to the total calorimeter enthalpy to account for the energy that was lost during deposition.

The calibration results after the correction function was applied are given in Table D.2. After the correction function was applied the uncertainty in the system was no longer systematic. For the tin calibration experiments the measured total enthalpy of the calorimeter varied ± 1.1% when the final calorimeter temperature was kept below 460 K (187 °C).

Calorimeter Validation

1.1 mm (0.045 in.) ER70S-6 steel welding wire was used to test the calorimeter against the other researchers who have measured droplet heat content of steel consumables. Electrode extension and arc length were held constant at 12.5 mm (0.5 in.). The shielding gas used was commercially pure argon. Figure 3.3 compares the results obtained in this study with previous researchers.

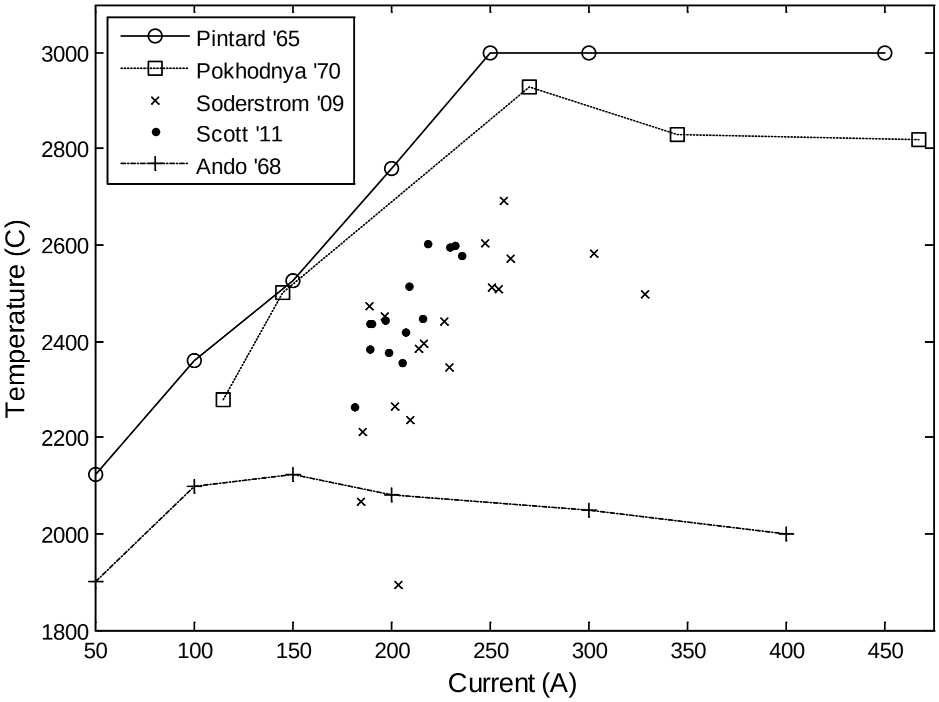

(a)

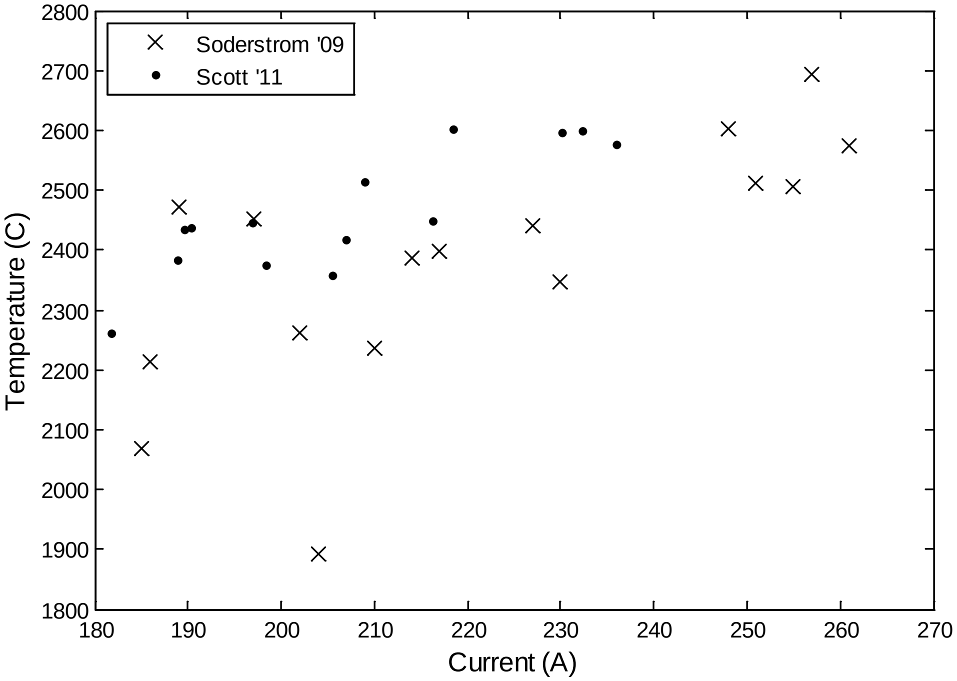

(b)

Figure 2.13 Droplet temperature measurements as they compare with other studies (a). Measurements as they compare with Soderstrom (b).

Temperature measurements from the solid state calorimeter compare well with those of Soderstrom, and are within reason of other researchers. In this study, the transition from globular to spray transfer occurs at approximately 205 A. The data indicate a minimum droplet temperature at this transition as reported by Soderstrom.

Chapter 3 : Heat Transfer in Tubular Consumables

The work presented in the literature review represents the cutting edge of droplet enthalpy quantification. All previous studies have used solid consumables in their analysis. It is necessary to quantify the effective thermophysical properties of tubular consumables to further understand and quantify the heat content of the droplets.

Typical alloy additions to Ni/WC wires include silicon, boron and chromium in very small amounts to increase weldability and improve alloy performance. Every manufacturer, however, adds these elements in varying quantities and in varying form. The one constant between these wires is that by mass the composition is nearly exclusively Ni, W and C. Therefore, for the purpose of this study it will be assumed that these wires are composed entirely of Ni, W and C.

Wire Composition

The carbide in the H.C. Starck Ni/WC wire exists in two general forms; WC and W_2C. To approximate how much of each is present in 100 g of wire, two equations must be solved simultaneously:

$$m_W^{wire} = (m_{W_2C})\left(f_W^{W_2C}\right) + (m_{WC})(f_W^{WC})$$
$$m_C^{wire} = (m_{W_2C})\left(f_C^{W_2C}\right) + (m_{WC})(f_C^{WC})$$

Equations 3.1-3.2

where $m_W{}^{wire}$ is the total mass of tungsten in 100 g of the wire, $f_W{}^{W2C}$ is the molar fraction of tungsten in W_2C, $f_W{}^{WC}$ is the molar fraction of tungsten in WC, $m_C{}^{wire}$ is the total mass of carbon in 100 g of wire, $f_C{}^{W2C}$ is the molar fraction of carbon in W_2C and $f_C{}^{WC}$ is the molar fraction of carbon in WC. The two unknowns in this system, m_{W2C} and m_{WC} represent the total mass of W_2C and WC in 100 g of the wire respectively. Using weight fraction data gathered by Stuart Guest [17] with ICP mass-spectroscopy analysis, Table 4.1 shows the calculated composition of the consumable. The volume fraction of carbides measured (36.1 vol.%) includes both WC and W_2C.

Table 3.1 Composition of H.C.Starck Ni/WC consumable as calculated by Equations 4.1 and 4.2. Although more species are present within the wire, Ni, W and C account for the majority of the wire by mass.

Element	*Mass in 100 g of Wire*	*Weight fraction (%)*	*Volume fraction (%)*	*Volume fraction (%)(measured)*
Ni	35.5	35.5	37.3	35.3
W	61.6	-	-	-
C	2.9	-	-	-
WC	-	28.98	17.1	36.1
W_2C	-	35.56	19.4	
Air	-	-	26	28.6

The powders in the core of the wire do not have a packing factor of 1; therefore, air is also considered in the volume fraction calculation. Using the density of bulk Ni, WC and W_2C and the known mass of each in 100 g of wire the total volume of each constituent was calculated.

Total wire volume was calculated by calculating the length of 100 g of wire using the linear mass and the average diameter of the wire. Subtracting the volume of nickel from the total volume of the wire leaves the total volume of the core. Further, subtracting the volume of Ni, WC and W_2C from the total wire volume yields the total volume of air in the core of the wire. This establishes a ratio between the amount of continuous phase (air) and the amount of solid phase (WC/W_2C) in the core of the wire. This becomes important when thermal conductivity is calculated in the Effective Thermal Conductivity section.

Based on typical W and C compositions in overlay alloys it was expected that the ratio of W_2C to WC should be approximately 2:1, but this was not seen in the calculated weight fractions. This was not expected to influence calculations since the two carbides have very similar properties.

Effective Enthalpy and Specific Heat Capacity

A tubular consumable is represented by the schematic in Figure 3.1. Here, the powder is represented by A_{powder} and the sheath by A_{Ni}. The total cross sectional area of the wire is:

$$A_{power} + A_{Ni} = A_{tot}$$

Equation 3.3

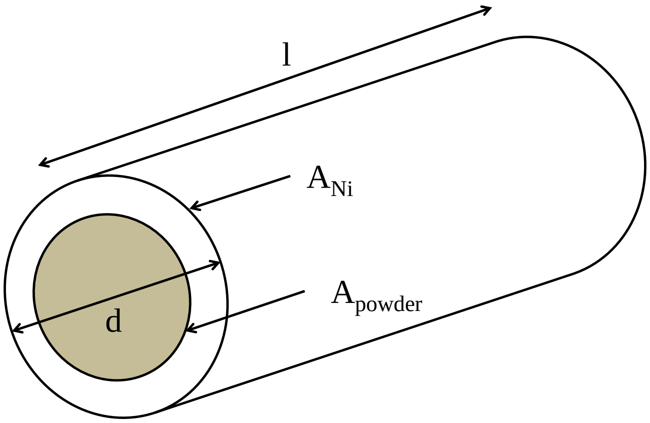

Figure 3.1 Schematic of an idealized tubular consumable. Although the sheath appears uniform in the Figure, the actual geometry of the cross section may change depending on processing conditions.

Considering a tubular wire with weight fractions given in Table 3.1 and total linear mass, ν_{tot} (kg/m), then:

$$\nu_{Ni} = (\nu_{tot})(\lambda_{Ni})$$
$$\nu_{WC} = (\nu_{tot})(\lambda_{WC})$$
$$\nu_{W_2C} = (\nu_{tot})(\lambda_{W_2C})$$

Equations 3.4-3.6

where λ and ν denote the weight fraction and linear mass of the respective constituent. The area, or volume, fraction, μ, of each constituent is calculated by:

$$\mu_{Ni} = \frac{\nu_{Ni}}{(\rho_{Ni})(A_{tot})}$$
$$\mu_{WC} = \frac{\nu_{WC}}{(\rho_{WC})(A_{tot})}$$
$$\mu_{W_2C} = \frac{\nu_{W_2C}}{(\rho_{W_2C})(A_{tot})}$$

Equations 3.7-3.9

where ρ is the bulk density in kg/m^3. The effective volumetric enthalpy, H_{eff}, can then be written as:

$$H_{eff} = (H_{Ni})(\mu_{Ni}) + (H_{WC})(\mu_{WC}) + \left(H_{W_2C}\right)\left(\mu_{W_2C}\right) + (H_i)(\mu_i)$$

Equation 3.10

where H_i (J/m^3) and μ_i are the volumetric enthalpy and area or volume fraction of any additional species present in the wire. Equation 3.10 is valid for the wire when no melting has occurred. Effective volumetric specific heat capacity follows by:

$$c_{p,eff} = (c_{p,Ni})(\mu_{Ni}) + \left(c_{p,WC}\right)(\mu_{WC}) + \left(c_{p,W_2C}\right)\left(\mu_{W_2C}\right) + \left(\mathrm{c}_{p,i}\right)(\mu_i)$$

Equation 3.11

The average specific heat capacity from room temperature to melting is 3.118E+06. Tables E.1 and E.2 summarize the temperature dependant density, volumetric enthalpy and specific heat capacity for Ni, WC and the tubular wire.

Effective Thermal Conductivity

Thermal conductivity is well tabulated for bulk materials with small levels of impurities. However, the mechanisms of heat transfer change when powder is one of the conducting materials. Surface asperities of the particles and the packing factor of the powder influence the effective thermal conductivity.

Tsotsas and Martin [30] conducted an extensive review of the thermal conductivity of packed beds in different configurations. The authors indicate primary and secondary factors for heat transfer in packed beds. Primary factors are the thermal conductivity of the dispersed (solid) phase, the thermal conductivity of the continuous (fluid) phase and the relative proportion of these phases in the mixture. Secondary parameters include the heat transfer through radiation of the particles, the pressure dependence of the thermal conductivity, heat transfer due to the flattening of the particles and heat transfer due to convection. Secondary factors were not considered when calculating the effective electrical resistivity because conduction is the only heat transfer mechanism with an electrical analogy. This becomes important in subsequent analysis when the Wiedemann-Franz law is employed. The equations used for considering only primary factors are described in the paper of Tsotsas and Martin. The following equations calculate the thermal conductivity of the powder in the wire when considering secondary factors. The ratio of the thermal conductivity of the packed bed (λ_{2ph}) to the thermal conductivity of the fluid phase (λ) is given by k_{2ph}:

$$k_{2ph} = \frac{\lambda_{2ph}}{\lambda}$$

Equation 3.12

where:

$$k_{2ph} = \left(1 - \sqrt{1-\psi}\right)\psi[(\psi - 1 + k_G^{-1})^{-1} + k_R] + \sqrt{1-\psi}[\varphi k_P + (1 - \varphi k_c]$$

Equation 3.13

with:

$$k_c = \frac{2}{N}\left\{\frac{B(k_P + k_R - 1}{N^2 k_G k_P} \ln \frac{k_P + k_R}{B[k_G + (1-k_G)(k_P + k_R)]} + \frac{B+1}{2B}\left[\frac{k_R}{k_G} - B\left(1 + \frac{1-k_G}{k_G} k_R\right)\right] - \frac{B-1}{N k_G}\right\}$$

$$N = \frac{1}{k_G}\left(1 + \frac{k_R - B k_G}{k_P}\right) - B\left(\frac{1}{k_G} - 1\right)\left(1 + \frac{k_R}{k_P}\right)$$

$$B = C_f \left[\frac{(1-\varphi)}{\varphi}\right]^{\frac{10}{9}} f(\zeta)$$

$$k_R = \frac{4C_s}{\frac{2}{\varepsilon} - 1} T^3 \frac{d}{\lambda}$$

$$k_p = \frac{\lambda_P}{\lambda}$$

$$k_G = \left(1 + \frac{l}{d}\right)^{-1}$$

$$d = \sum \left(\frac{Q_i}{d_i}\right)^{-1}$$

$$f(\zeta) = 1 + 3\zeta$$

$$\zeta = \left[\frac{\sum Q_i / d_i^2}{\left(\sum Q_i / d_i \right)^2} - 1 \right]^{0.5}$$

Equations 3.14-3.22

where ψ is the bed porosity, or the ratio of air to total volume in the core of the wire and λ_p is the thermal conductivity of the bulk solid phase. The symbols and constants from Equations 3.14-3.21 are described in Table 3.2.

Table 3.2 Constants and symbols used in Equations 3.12-3.21 as described by Tsotsas and Martin. The flattening coefficient and shape factor are taken from [30] and emissivity of the solid phase from [31].

Symbol	*Definition*	*Notes*
λ_{2ph}	Thermal conductivity of the packed bed	
λ	Thermal conductivity of the cont. phase	
ψ	Bed porosity	
φ	Flattening coefficient	From [30] Table 2
λ_p	Thermal conductivity of the solid phase	
C_f	Shape factor	From [30] Table 2
C_s	Radiation constant of the blackbody	5.67E-8 W/m^2K^4
T	Absolute temperature	
ε	Emissivity of the solid phase	For WC, from [31]
l	Characteristic length of solid particle	
d	Mean particle diameter	
Q_i	Volumetric proportion of the ith fraction in the bed	
d_i	Particle diameter of the ith fraction in the bed	

Combining the thermal conductivity of the powder with the thermal conductivity of the Ni sheath yields the overall thermal conductivity of the wire given in Equation 3.23. The area fraction of the powders was consolidated because inadequate data exists for W_2C. Therefore, it was assumed that the thermal conductivity of the WC/W_2C powder was the same as a WC powder.

$$\lambda_{eff} = (\mu_{Ni})(\lambda_{Ni}) + (1 - \mu_{Ni})(\lambda_{2ph})$$

Equation 3.23

Average thermal conductivity from room temperature to melting is 28.3 W/mK.

Effective Electrical Resistivity

The Ni sheath and WC/W_2C powder can be considered parallel resistors. The total resistance of the two resistors is given by:

$$\frac{1}{R_{tot}} = \frac{1}{R_{Ni}} + \frac{1}{R_{Powder}}$$

Equation 3.24

Equation 3.24 can be expressed as:

$$\frac{A_{tot}}{(\rho_{r,tot})(l)} = \frac{A_{Ni}}{(\rho_{r,Ni})(l)} + \frac{A_{Powder}}{(\rho_{r,Powder})(l)}$$

Equation 3.25

where ρ_r is the electrical resistivity of the bulk material and l is the length of the conductor. In the case of the electrode, l is the electrode extension. The area of each of the constituents is given by:

$$A_{Ni} = (\mu_{Ni})(A_{tot})$$
$$A_{Powder} = (\mu_{WC} + \mu_{W_2C})(A_{tot})$$

Equations 3.26-3.27

Replacing Equations 3.26-3.27 into Equation 3.25 and manipulating the structure of the equation leaves:

$$\rho_{r,tot} = \left(\frac{\mu_{Ni}}{\rho_{r,Ni}} + \frac{(\mu_{WC} + \mu_{W_2C})}{\rho_{r,Powder}}\right)^{-1}$$

Equation 3.28

The electrical properties of the materials used in this study were not readily available, therefore the Wiedemann-Franz Law [32] was used to approximate electrical resistivity of the bulk materials based on thermal conductivity. Although valid for metallic elements, this approximation was also used for WC because no better data was available. This relationship is given by:

$$\lambda\rho_r = \frac{\pi^2 k_b^2}{3e^2} T$$

Equation 3.29

where λ is the thermal conductivity, ρ_r is the electrical resistivity, k_b is Boltzmann's constant, e is the charge of an electron and T is the absolute temperature. Good agreement between calculated and measured electrical resistivity was achieved as seen in Figure 3.2.

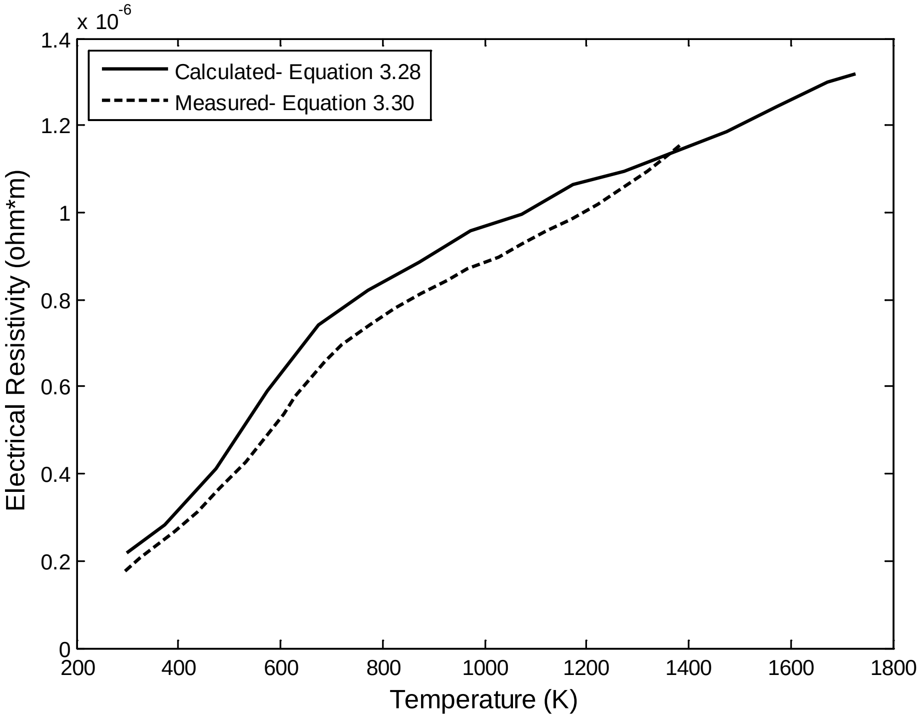

Figure 3.2 Calculated effective electrical resistivity compared to measured values for the H.C. Starck 1.6 mm consumable.

Total wire resistance was measured by measuring the voltage drop of a known length of wire when 5A current was passed through. The wire was placed in a furnace at a known temperature. Resistivity was calculated from Equation 3.30 using known wire dimensions.

$$\rho_r = \frac{R_{tot} A_{tot}}{l}$$

Equation 3.30

where R_{tot} is the total measured resistance in Ω and A_{tot} is the total conductor cross sectional area in m^2 calculated from average wire diameter measurements. Average calculated resistivity from room temperature to melting is 8.905E-07 Ωm.

Temperature-dependant thermal conductivity and electrical resistivity data for Ni, the carbide powder and the overall wire are given in Appendix E, Tables E.3-E.4.

Chapter 4 : Theory of Droplet Heat Content

Two different energy balances were considered in this work to predict droplet heat content. One focused on the wire and droplet as a system, and the other focused on the energy input and losses of an individual droplet. For these predictions, the system was assumed to have reached steady state and did not consider highly-transient arc starts or extinctions. Results of these analyses are presented in Chapter 5.

Balance 1: Droplet/Electrode System Energy Balance

The energy balance of the droplet/electrode system in GMAW is presented in Figure 4.1.

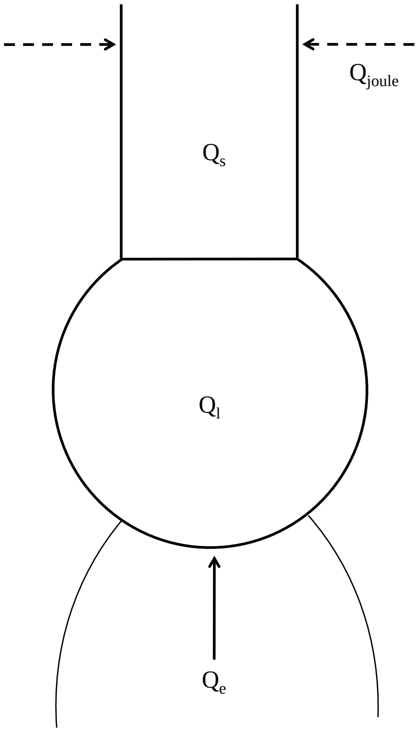

Figure 4.1 Representation of energy inputs when considering the droplet and electrode as a system. Energy in is balanced with the heating, melting and superheating of the electrode material.

In Figure 4.1, Q_e is the energy input by electron condensation at the anode spot, Q_{joule} is the energy input by Joule heating in the electrode extension of the wire, Q_s is the heating and melting of the wire and Q_l represents the superheating of the droplet. This balance represents an approximate approach that does not take into account the temperature dependence of material properties or heat losses by radiation, convection or vaporization This balance is similar to the one used by Ma and Apps [12] and is expressed by:

$$Q_{joule} + Q_e = Q_s + Q_l$$

Equation 4.1

It is important to note that the above balance does not take into consideration vaporization, the importance of which will be addressed in the discussion.

Electron Condensation

Anodic heat input can be divided into three terms; the anode fall voltage, the electronic work function of the electrode material and the energy released by the electrons transitioning from a high energy state in the plasma to a lower energy state in the liquid. The equation takes the form:

$$Q_e = i\left[\varphi^\circ + \frac{2k_b T_e{}^\circ}{e} + \varphi_m\right]$$

Equation 4.2

where i is the welding current, φ° is the anode fall voltage, k_b is Boltzmann's constant, $T_e{}^\circ$ is the electron temperature at the anode spot, e is the charge of one electron and φ_m is the work function of the anodic material. Equation 4.2 is taken from Krivtsun *et al.* [33]; however, several other researchers report different constants before the electron condensation term [34-37], and some leave the anode fall voltage out of the calculation completely [35, 38]. Also, because metal vapor exists in the plasma there is uncertainty in the electron temperature.

Typical values for the total volt equivalent have been reported to be around 5-7 V for aluminum and steel [16, 20, 34]. When considering only electron condensation at 9900 K and the work function of pure nickel, the value is approximately 7 V.

Joule Heating

Some energy transferred through the electrode is dissipated as heat and is proportional to the total resistance of the conductor and the square of the current passing through. Joule heating is represented by:

$$Q_{joule} = I^2 R$$

Equation 4.3

Heating, Melting and Superheating

The energy inputs from Equation 4.1 are balanced with the heating, melting and super heating of the electrode and droplet. They are calculated by:

$$Q_s = (\Delta H_{solid})u$$
$$Q_l = \left[H_{fus} + (H_l - H_m)\right]u$$

Equations 4.4-4.5

where ΔH_{solid} is the enthalpy change of the electrode from room temperature to its melting temperature, H_{fus} is the enthalpy of fusion, H_l is the enthalpy of the droplet at its initial temperature, H_m is the enthalpy of the molten droplet at its melting temperature and u is the melting rate of the electrode.

Balance 2: Energy Balance at Droplet

The second energy balance considered in this study was the energy balance at the droplet. This balance is presented in Figure 4.2.

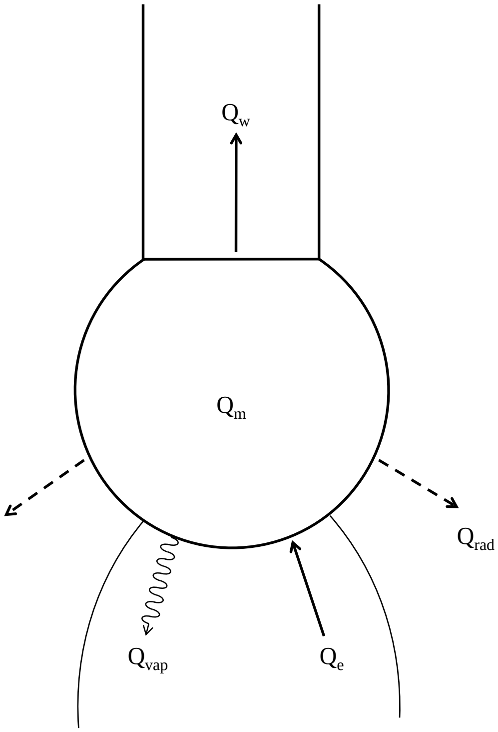

Figure 4.2 Representation of energy inputs and energy losses in the molten droplet in GMAW.

The energy input in Figure 4.2, Q_e, described in Equation 4.2, represents the energy delivered to the droplet by the electrons condensing at the anode spot. Q_w, Q_{rad} and Q_{vap} is heat loss by conduction into the wire, heat loss by radiation and heat loss by vaporization respectively. Q_m is the overall heat accumulation in the droplet. This balance is shown in Equation 4.6:

$$Q_m = Q_e - (Q_w + Q_{rad} + Q_{vap})$$

Equation 4.6

where the unit of each term is W. In this case it was assumed that radiation losses while the droplet is still attached to the electrode are negligible compared to the other heat inputs and losses.

Heat Loss to the Electrode

The most significant heat loss from the droplet while it is attached to the electrode is due to conduction into the wire. The model of Lehnhoff and Mendez [39] calculates Q_w while considering the non-linear effects of thermophysical properties with temperature by solving the governing equation:

$$\frac{d}{dx}\left(\alpha\frac{dH}{dx}\right)+u\frac{dH}{dx}+\frac{\rho_r I^2}{A^2}-2\frac{\sigma\epsilon}{r}\left(T^4-T_\infty^4\right)-2\frac{h}{r}\left(T-T_\infty\right)=0$$

Equation 4.7

Using the boundary conditions:

$$H(0)=H_m$$
$$H(l)=H_o$$

Equations 4.8-4.9

The first term in Equation 4.7 represents conduction from the molten droplet into the electrode, the second term is advection due to the wire being fed at speed *u*, the third term is heating of the wire in the extension region due to the Joule effect and the fourth and fifth terms represent heat loss by radiation and convection to the room temperature surroundings. In Equations 4.4-5, *H*(0) refers to the enthalpy of the wire at the melting interface while *H*(*l*) represents the enthalpy of the wire at the contact point between it and the contact tip. Figure 4.3 shows the configuration used for Lehnhoff's work.

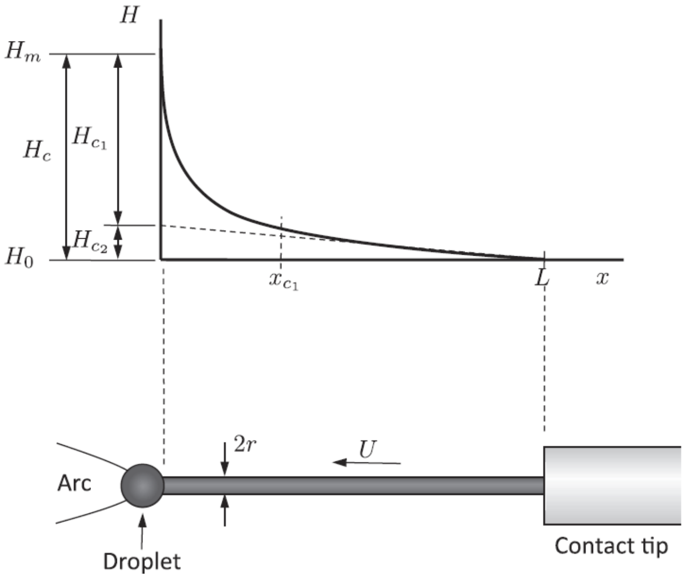

Figure 4.3 Configuration used by Lehnhoff and Mendez [39]. The graph shows how the total enthalpy of the wire at the melting interface (H_c) is sectioned into heating by Joule heating (H_{c2}) and heating by conduction (H_{c1}).

A Matlab program written by Lehnhoff coupled with the internal bv4pc adaptive finite difference code was used to solve Equation 4.7 for the Ni/WC tubular wire using the effective values for enthalpy, heat capacity, electrical resistivity and thermal conductivity.

Heat Loss by Vaporization

The influence of vaporization on the overall energy balance of the droplet is not well understood or agreed upon. Some researchers used a method based on the Langmuir vaporization rate equation and reported vaporization powers on the order of 1000 W [6, 40], while Soderstrom used a semi-empirical model developed by Deam *et al.*[41] and obtained vaporization power on the order of 50-200 W. The Langmuir method assumed vaporization into a vacuum, which may not be accurate depending on the species present in the plasma. This would lead to an overestimation of the vaporization rate. In this study the Langmuir evaporation equation was used assuming the temperature at the anode never exceeds boiling. This is only an estimation, as the actual temperature at the anode can exceed the boiling point of the electrode material and changes from case to case [6]. Langmuir evaporation is given by [42]:

$$Q_{vap} = A_a H_{vap} \beta P \sqrt{\frac{M_w}{2\pi R T_a}}$$

Equation 4.11

where A_a is the anode spot area, H_{vap} is the heat of vaporization of the electrode material, β is a correction factor taken from Haidar [40], P is the partial pressure of metal vapor at the anode spot, M_w is the molecular weight of the electrode material, R is the universal gas constant and T_a is the surface temperature at the anode spot. Vaporization does result in very small changes in the droplet diameter, but this was considered negligible compared to the total droplet diameter.

Heat Accumulation

The heat accumulation term from Equation 4.6 is the melting and super heating of the droplet from the melting temperature to the temperature of the droplet as it is detached from the electrode. It is described by Equation 4.12:

$$Q_m = u A_w \Delta H_{fus} + V_{drop} f_d \left(H_{T_i} - H_{T_m} \right)$$

Equation 4.12

where u is the wire feed speed, V_{drop} is the volume of the molten droplet, f_d is the droplet detachment frequency. H_{Ti} is the enthalpy of the droplet as it is detached from the electrode and H_{Tm} is the enthalpy of the liquid droplet at the melting temperature.

Although very similar, the two proposed balances differ in that one considers the heat input to the droplet/wire system through Joule heating while the balance considering only the droplet considers heat loss from the droplet by conduction into the wire. Another significant difference is that one considers vaporization from the anode spot while the others do not. As mentioned, there is substantial debate as to whether or not vaporization is significant in the overall heat balance. Vaporization is discussed in the Synthesis of Heat Balance Results section.

Chapter 5 : Results and Discussion

Results and discussion for the three aspects of the current study are given below along with the experimental procedure followed prior to performing the experiments. Experimental results are presented, followed by bead-on-plate trials and droplet heat content prediction.

Experimental Procedure

The following steps outline the procedures followed to consistently perform experiments in this study:

1. Switch the power supply to the "on" position, open valve on the shielding gas.
2. Allow the machine to perform its self-diagnostic tests until the wire feeder displays the voltage and wire feed speed settings.
3. Activate the water pump for the water-cooled copper cathodes closed-loop cooling system. If catholic power inputs will be calculated, set the flow rate to the necessary value using the gate valve and the in-line flow meter.
4. Use a die grinder equipped with an abrasive disk to clean the through-hole thoroughly, ensuring a clean, uniform surface.
5. Position the torch in the center of the cathode using the X-Y-Z manipulator. The wire can be cold-fed using the "Jog" toggle switch located on the wire feeder to ensure the wire will feed through the center of the through-hole. Using the 25.4 mm (1 in.) block indicator check that CTWD is 25.4 mm. Adjust as necessary.
6. Using the 12.5 mm (0.5 in.) block adjust the tungsten indicator so that it sits 12.5 mm above the top plane of the through-hole.
7. Clip excess wire with side cutters so the tip of the wire is just above the top plane of the through-hole.
8. Position a small strip of aluminum foil across the through-hole.

9. Position the calorimeter 12.7 cm (5 in.) below the bottom plane of the through-hole.
10. Use the “Purge” toggle switch on the wire feeder to check that the flow rate of the shielding gas is set to the desired value. To adjust, turn the control valve on the rotameter clockwise to decrease flow or counterclockwise to increase flow.
11. Open both LabView and Daqview for current/voltage and temperature data acquisition. Prepare both windows for triggering.
12. Set the power switch for the current and voltage transducers to “on”.
13. Position the frame for the tinted welding glass in such a way that it blocks the arc light, but allows the user to easily see the wire feeder controls and data acquisition computer.
14. Position catch basin over the calorimeter.
15. Use the remote activation switch to engage the arc. Adjust voltage and wire feed settings until arc length matches the tungsten indicator.
16. Disengage the arc, follow steps 4-9 to prepare the surface for the experimental run.
17. Remove the catch basin to expose the surface of the calorimeter.
18. Trigger Daqview to begin collecting temperature data.
19. Engage the arc using the remote activation switch.
20. Ensure the process is stable, then trigger Labview to collect current and voltage data. End current/voltage acquisition after several seconds of collection.
21. Disengage the arc.
22. Cover the calorimeter with fiberfrax insulation to contain as much heat as possible.
23. End Daqview data collection when the temperature of the calorimeter has reached a maximum and has begun to decline.
24. Data are now ready for analysis in Matlab.

Experimental Results

The results of the experimental portion of this study are shown in Figure 5.1. A minimum average droplet heat content was observed in the transition between the equivalent of globular and spray transfer.

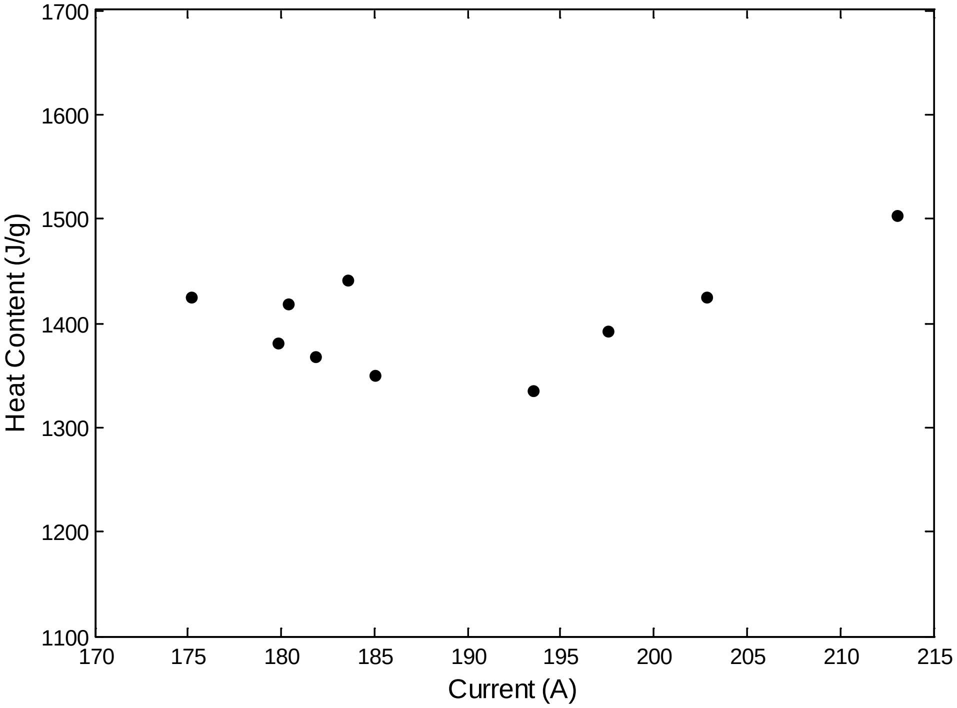

Figure 5.1 Average droplet heat content vs. average welding current for the HC Starck CTC NI/WC wire. Results indicate a minimum droplet heat content at approximately 190 A.

Several aspects of Figure 5.1 are worth noting. First, the data collected at low current shows more scatter than those at high current. Second, a minimum in droplet heat content was seen between 185 and 195 A. Third, unlike solid wire the transition occurs over a broad range of welding current. These features are described in subsequent analysis.

Arc Stability

The difference in arc behavior between solid and tubular consumables is drastic. When calibrating the calorimeter with steel wire, the arc was predictable and detachment events occurred regularly. However, with the Ni/WC wire this was not the case. The anode and cathode spots were very mobile leading to unpredictable detachment events. Unlike solid wires, there is no distinct transfer mode with tubular consumables. As such, even in globular transfer small droplets were occasionally generated and in the spray transfer region large droplets were formed intermittently.

The dynamics of droplet detachment are complex and depend on the transfer mode. In globular transfer, the dominant forces that are involved in droplet detachment are gravity and the capillary force of the liquid metal on the solid electrode that opposes gravity. Another consideration in globular transfer is the effect of the vapor pressure at the anode spot which can also act to oppose gravity. In spray transfer gravity, capillary action and plasma shear stresses play a role, but the dominant force is the "pinch" effect caused by the force that results from the high current flowing through the plasma, droplet and wire and the induced magnetic field surrounding the conductors. This effect is described by Lancaster [37] and is governed by Equation 5.1.

$$F = j \times B$$

Equation 5.1

where F is the resulting force, j is the current density and B is the magnitude of the induced magnetic field. Typically the anode spot is slightly larger than the wire diameter leading to a divergent current path. This geometry leads to a resultant force that is directed radially inward and slightly downward. The inward component of the force vector acts to pinch the wire, propagating the pinch effect even further by increasing the current density until the droplet is detached. The other component of the force vector creates a net downward force that creates a plasma jet that accelerates the droplet into the arc column. This phenomenon has been studied and modeled by many researchers [37, 43-45] among others. The difference in arc attachment configuration between solid and tubular wires is shown below in Figure 5.2.

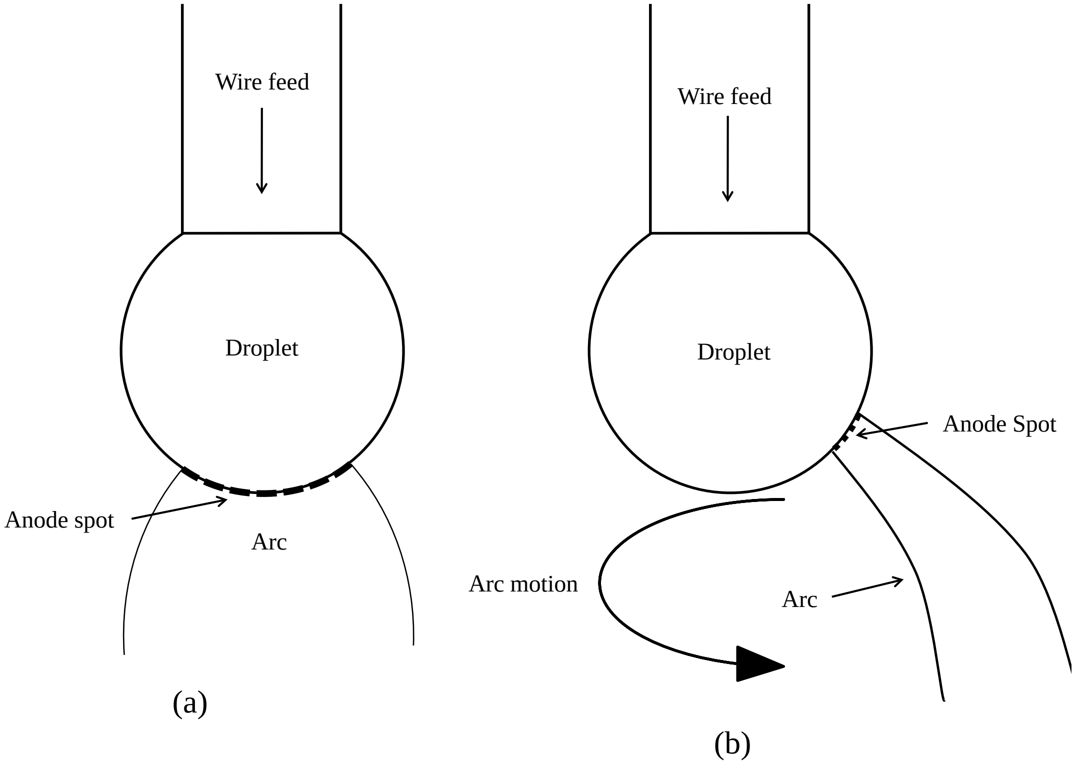

Figure 5.2 Arc configuration in globular transfer for a solid consumable (a) compared to that for a tubular wire (b).

In Figure 5.2 (a) the anode and cathode spots remain stable. The only change in the attachment point comes when current is increased and the arc begins to envelope the droplet (in an argon rich atmosphere), causing the transition from globular to spray transfer mode. In the tubular case, however, it is possible that the anode spot is erratic and unpredictable due to the uneven melting of the Ni sheath and inconsistencies within the powder in the core of the wire. These inconsistencies lead to irregular metal transfer and “mixed” transfer modes that explain why, in Figure 5.1 there are two points that lie outside the trend. In these cases it is possible that the average droplet size was larger than others in the globular transfer mode. When welding current increases beyond the transition, transition becomes more predictable; therefore, droplet heat content followed the expected trend.

To demonstrate the difference in arc stability between solid ER70S-6 and tubular Ni/WC wires, a Fast Fourier Transform (FFT) of the voltage signal for each is shown in Figure 5.3.

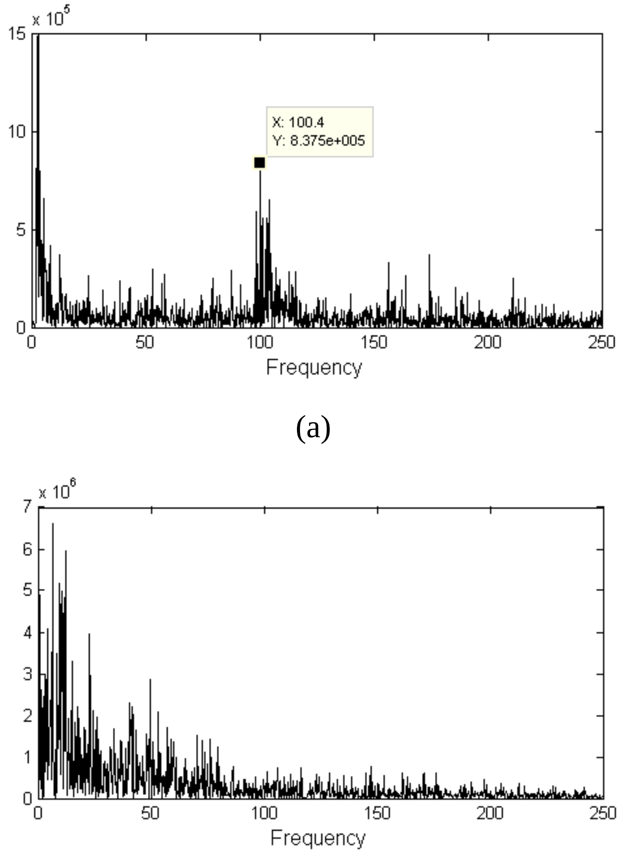

(a)

(b)

Figure 5.3 FFT for ER70S-6 electrode (a) and Ni/WC tubular wire (b). A distinct peak is seen for the steel consumable at 100 Hz, but no such peak is seen for the Ni/WC wire.

For solid consumables for which detachment events are predictable, each detachment leads to a spike in the voltage signal. These spikes occur at regular intervals and are represented by a sharp peak in the FFT (Figure 5.3a). When detachment events do not occur regularly and are unpredictable, the FFT response is not as sharp, and does not indicate any preferred detachment frequency.

Droplet Temperature

Initial calculations of droplet temperature yielded average temperatures that were several hundred degrees above the boiling point of nickel. These calculations were conducted using Equation 3.10 which considers the case where there is no mixing between the powders and the sheath. This may not be realisitc for Ni/WC consumables, however, due to the affinity for the powders to dissolve in molten nickel. For comparison, an equilibrium Thermocalc enthalpy vs. temperature curve was calculated with W, C and Ni in the weight fractions present in the CTC wire using the TTNi8 database. Figure 5.4 shows how the Thermocalc calculation compares to Equation 3.10.

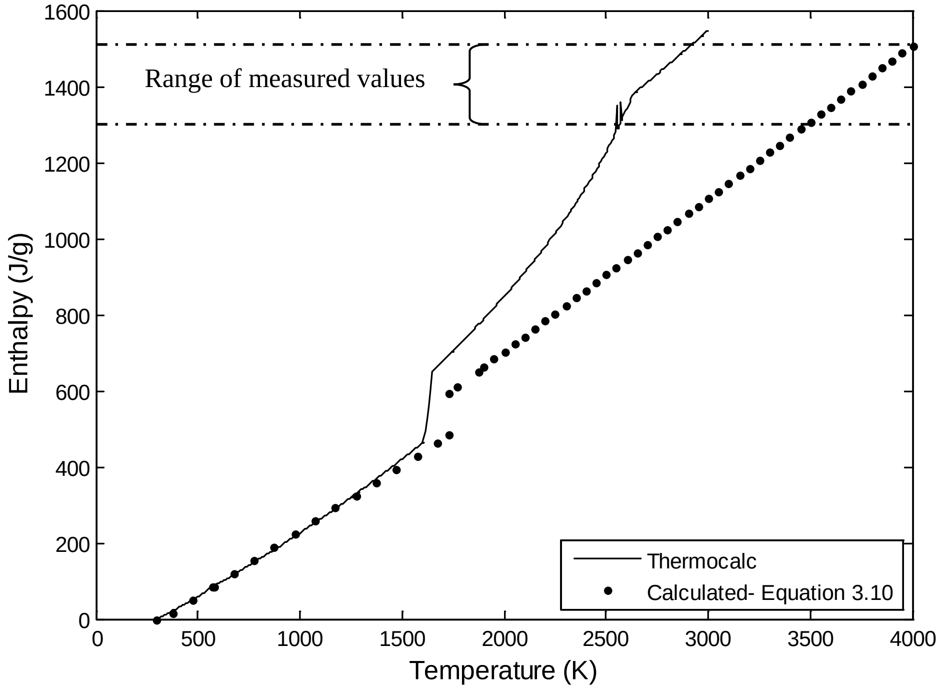

Figure 5.4 Thermocalc equilibirum enthalpy prediction compared to the no-mixing solution proposed in Equation 3.10.

There are two significant discrepancies between the curves. First, the melting temperature and heat of fusion are substantially different due to the presence of tungsten in the matrix in the equilibrium model. Second, at high temperatures the heat content varies significantly. This discrepancy alone can lead to 500-1000 degree temperature differences. Quantification of the amount of carbide dissolution is difficult due to secondary carbides re-precipitating from the matrix upon cooling. Therefore, to quantify droplet temperature information is needed about the amount of WC that was dissolved into the matrix, the volume fraction of secondary carbides, the composition of the secondary carbides and the heat of re-precipitation. Quantification of these parameters was not included in this study.

Time Dependant Heat Loss

The effect of uncertainty in the tabulated copper enthalpy and how it influenced the measured enthalpy was discussed in a previous section. The time dependant heat loss is another consideration that should be analyzed to ensure that it is either insignificant or significant and accounted for.

In the steel calibration trials, the maximum temperature reached by the calorimeter was 449 K (176 °C). Based on the heat loss during the tin calibration at a calorimeter temperature of 433 K (160 °C), the enthalpy loss rate is 5 W. The time it took the calorimeter to reach maximum temperature in the steel trial from the time the deposition ended was 176 sec. Therefore, the total heat loss due to the calorimeter sitting idle equates to 880 J when the total calorimeter enthalpy was approximately 38,000 J, or 2% of the total calorimeter enthalpy. This represents the worst-case scenario; in the Ni/WC trials the temperature of the calorimeter did not exceed 359 K (86 °C). At these temperatures the heat loss rate was less significant. As such the time dependant heat loss was neglected in the overall enthalpy calculations.

Energy Gain/Loss in Flight

In this work the droplets traveled further outside the arc than in a typical GMAW operation. The droplets traveled through two regions that impact droplet heat content after they are detached; the arc column and the region between the bottom of the cathode and the calorimeter. One concern is that excessive droplet energy gain/loss was occurring while the droplets were in flight. The mechanism for this loss would be mostly radiation and convection, expressed by:

$$Q_{rad} = \begin{cases} A_{drop}\varepsilon_{Ni}\sigma(T^4 - T_\infty^4) & (Outside\ arc\ column) \\ A_{drop}\varepsilon_{Ni}\varepsilon_{plasma}\sigma(T^4 - T_\infty^4) & (Inside\ arc\ column) \end{cases}$$

$$Q_{con} = h(T - T_\infty)\ (Inside\ and\ outside\ arc\ column)$$

Equations 5.2-5.3

where Q_{rad} is the rate of energy loss by radiation, A_{drop} is the surface area of the droplet, ε is the emissivity of molten nickel or argon plasma [46, 47] , σ is the Stefan-Boltzmann constant, Q_{con} is the rate of convective energy loss and h is the convection coefficient calculated from [48]. T is the average droplet temperature and T_∞ is ambient temperature. When the droplet was outside the arc column it was assumed to radiate to a black body, but inside the arc column the emissivity of the plasma was taken into consideration. Due to the complications encountered while calculating droplet temperature, it was estimated to be 2800 K. This value for temperature is consistent with the measured enthalpy values from Figure 5.4. The ambient temperature below the cathode was 298 K, while inside the plasma the temperature was assumed to be 9900 K. The parameters that were used for this calculation are given in Table 5.1.

Table 5.1 Parameters used for estimating energy gain/loss from the droplet after it was detached from the electrode.

Parameter	*Symbol*	*Unit*	*Value*
Electrode to cathode distance	-	mm	12.5
Cathode to calorimeter distance	-	mm	127
Emissivity of molten nickel	ε	-	0.3
Emissivity of argon plasma	ε	-	0.1
Droplet temperature	T	K	2800
Plasma temperature	T	K	9900
Convection coefficient	H	W/m^2K	39.4
Ambient temperature	T_∞	K	298
Stefan-Boltzmann constant	σ	W/m^2K	5.67E-08
Typical droplet area	A_{drop}	m^2	6.2E-05
Droplet velocity	-	m/s	1

Using a droplet velocity of 1 m/s [49], it was determined that above the cathode (in the plasma) the enthalpy of each droplet would be increased by approximately 13 J, while below the cathode the droplets would lose close to 10 J, resulting in a net gain of 3 J/droplet. If the average droplet heat content was estimated to be 1400 J/g with a droplet diameter of 0.002 m, the total enthalpy per droplet is on the order of 200 J. From this analysis it was concluded that the increased travel distance to the calorimeter did not significantly influence droplet heat content.

Synthesis of Heat Balance Results

From Equations 4.1 and 4.6 the average droplet heat content was predicted based on the thermophysical properties of the Ni/WC wires and known welding parameters established in the experimental portion of this work. The results are shown in Figure 5.7.

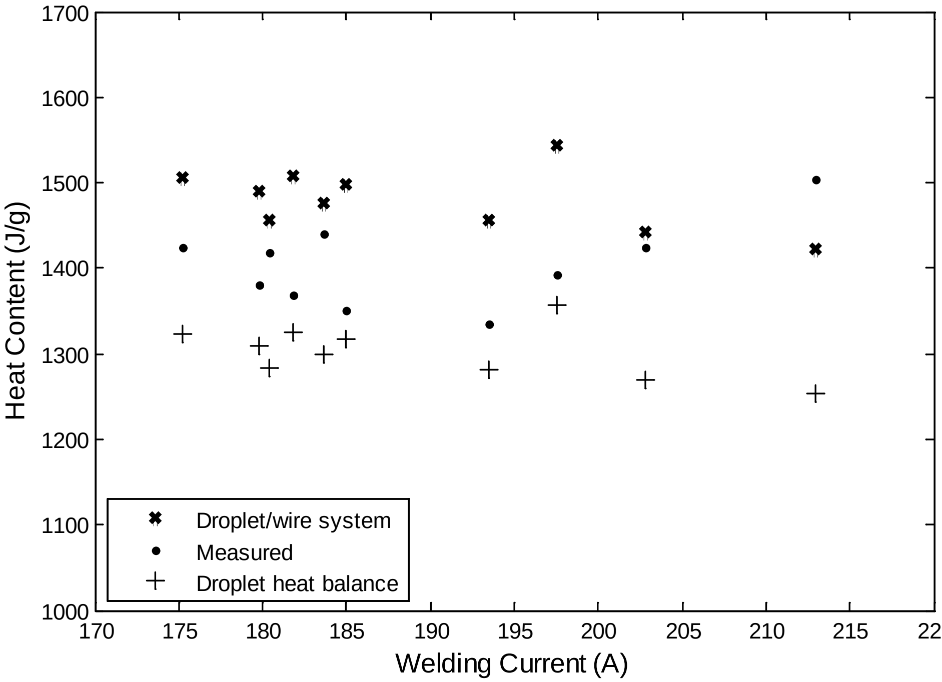

Figure 5.5 Predicted average droplet heat content compared to the measured droplet heat content. Results show good correlation.

Both predictions show the same trend. When vaporization was considered the predicted average droplet heat content was lower than both the measured values and the other prediction.

One of the most significant uncertainties in predicting droplet heat content was the energy input by electrons condensing on the droplet at the anode spot. As mentioned, there is substantial uncertainty in the constants and what terms should be included in the overall equation. The anode fall voltage can vary anywhere between 1-5 V [37] and is sensitive to arc attachment geometry as well as the temperature of the anode spot.

Another uncertainty lies with the work function of the electrode material. In this case it was assumed that electron transport was occurring only in the molten nickel, therefore only the work function of pure nickel was taken into account. The work function is highly impurity dependent, and tungsten and carbon are dissolving into the nickel matrix. The deviation in the work function can be up to 1 V [37].

There is also uncertainty in electron temperature in the near anode region. Although commercially pure argon was used as a shielding gas, the resulting plasma is not composed of pure argon due to metal vapors being present. The effect of these vapors lowers the temperature by increasing the radiative emission of the plasma, but the extent to which the temperature is lowered is unknown. For this case the temperature was estimated to be 9900 K based on work by Krivtsun [33], but temperatures have been estimated to be anywhere from 4,000-13,000 K [50, 51] when metal vapor is present.

The combination of uncertainties explains why there are discrepancies between the predicted droplet heat content and the measured droplet heat content as well as why there are inconsistencies between data in the predicted heat content. In the prediction the work function, electron temperature and anode fall voltage were kept constant for each trial. However, arc instabilities inherent with tubular consumables render the change in these properties unpredictable.

The model that predicted droplet heat content based on the heat balance at the droplet considered, although not completely, vaporization. The temperature at the anode spot and anode spot area were assumed to be the same in all cases, but practically this is not the case. As welding current increases in an argon rich plasma the arc will expand due to its relatively low thermal conductivity and begin to envelope the droplet and electrode. This expansion changes the attachment geometry of the arc to the droplet, the size of the anode spot and the location of electron condensation. All three factors will influence vaporization rate.

There is one subtle and one distinct difference between the two methods used for predicting droplet heat content. The subtle difference is the change from point to point. Although similar in each case, they are not the same. This is due to the thermal dependence of material properties taken into account in the droplet heat balance (Equation 4.6), but not in the electrode/wire system (Equation 4.1). The difference indicates that temperature-dependant properties are of secondary importance in the electrode extension region.

The distinct difference is due to two factors: vaporization and conductor area. Including vaporization in the estimation lowers the prediction relative to the model that does not consider vaporization. Both methods incorporated heat input by electron condensation, but one model added the energy input by Joule heating while the other considered energy loss by conduction into the wire. Energy loss by conduction is dependent on the conductor area. In the case of tubular wires conductor area is ambiguous not only because the core of the wire contains air, but also because it is possible the packing of the wire is not uniform. Therefore, conduction from the droplet into the wire changes with time and welding conditions.

Bead on Plate Trials

The minimum average droplet heat content was observed under ideal conditions where many of the typical variables in GMAW were controlled. Bead on plate trials were completed to confirm carbide survival with machine parameters that produced the minimum droplet heat content and at machine parameters that produced higher droplet heat content. The parameters were chosen based on the WFS and voltage settings of the machine that yielded the results shown in Figure 5.1. The parameters of the bead on plate trials are given in Table 5.2.

Table 5.2 Parameters used for bead on plate overlays. Travel speed was selected to keep heat input similar to that of Choi *et al.* [11]. Contact tip to work distance was maintained at 25.4 mm (1.0 in.). The current reported is approximate.

Trial number	*WFS (in/min)*	*Current (A)*	*Voltage (V)*	*Travel speed (in/min)*	*Notes*
20110406001	172	194	26.9	17.5	At minimum
20110406002	172	194	26.9	17.5	
20110407001	196	213	26.9	17.5	Above minimum
20110407002	196	213	26.9	17.5	

The shielding gas used was commercially pure argon. Figures 5.5 and 5.6 show the resulting bead appearance and macrostructures of the overlay deposits.

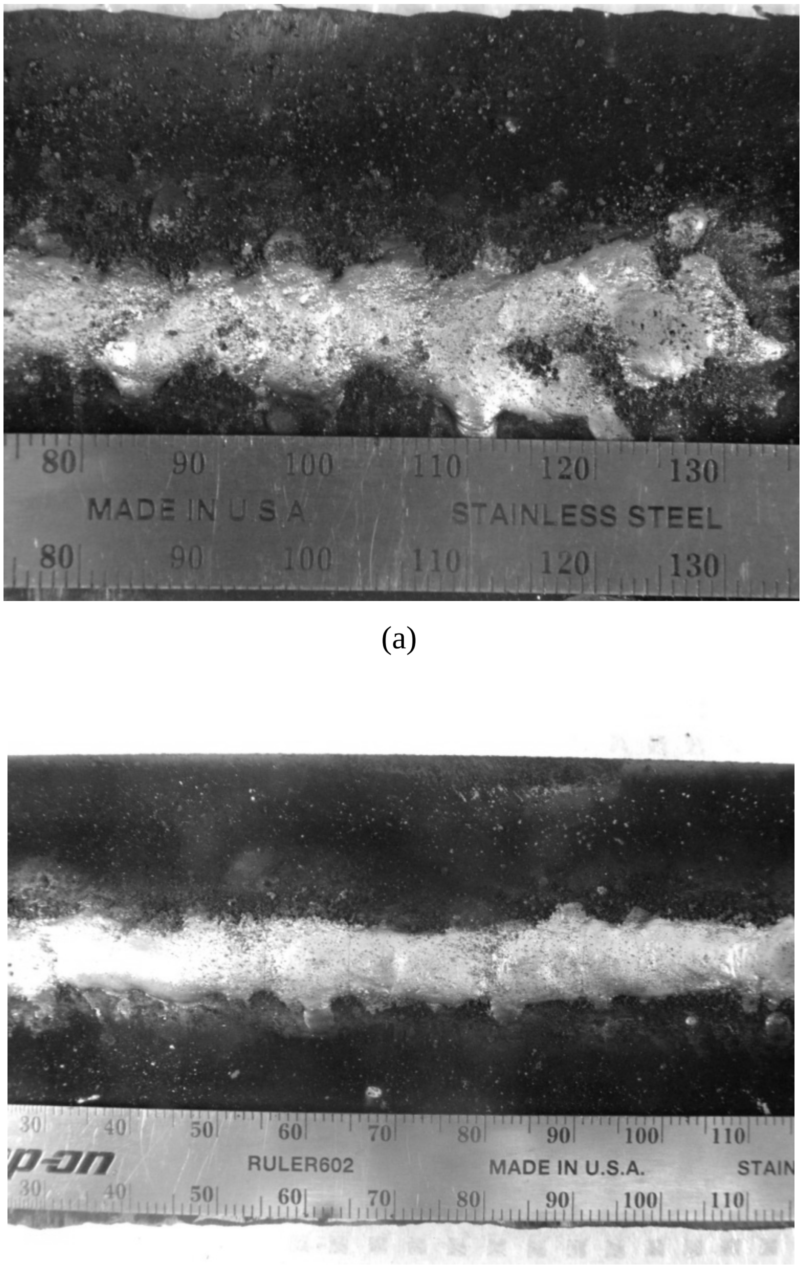

(a)

(b)

Figure 5.6 Bead appearance after deposits at the minimum (a) (194 A) and above the minimum (b) (213 A). Note the better bead appearance at higher currents.

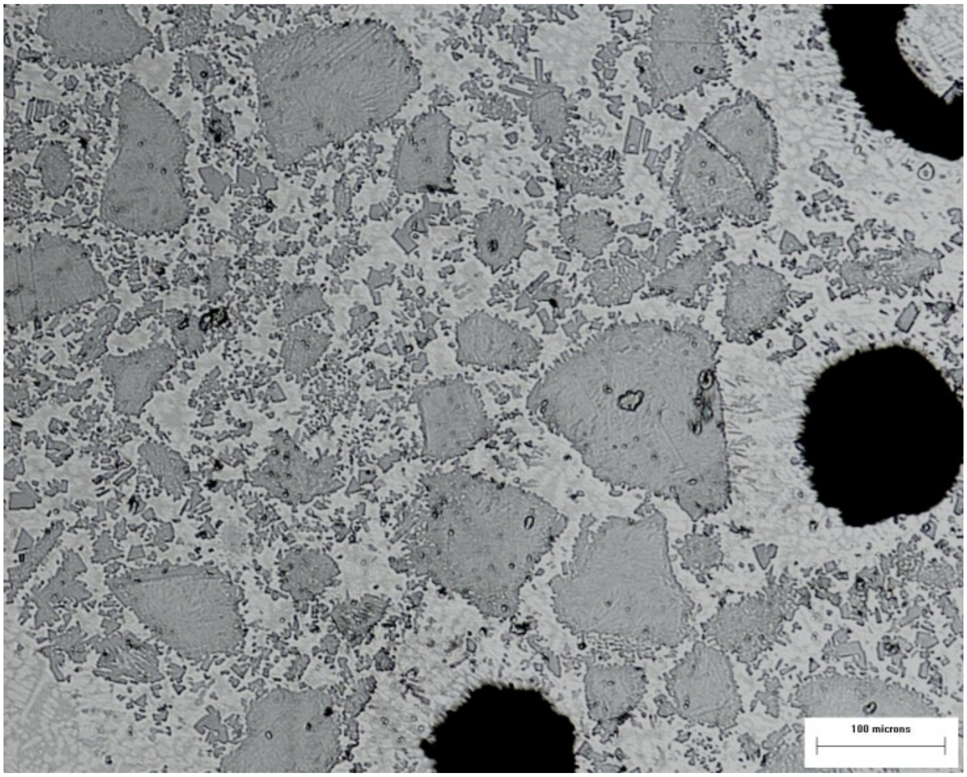

(a)

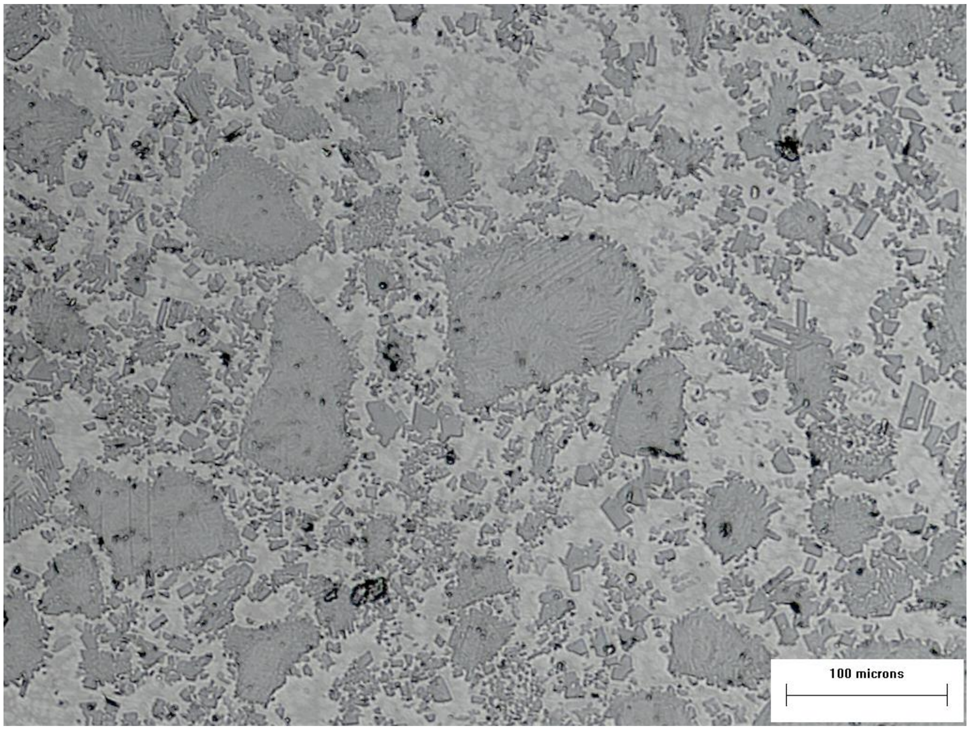

(b)

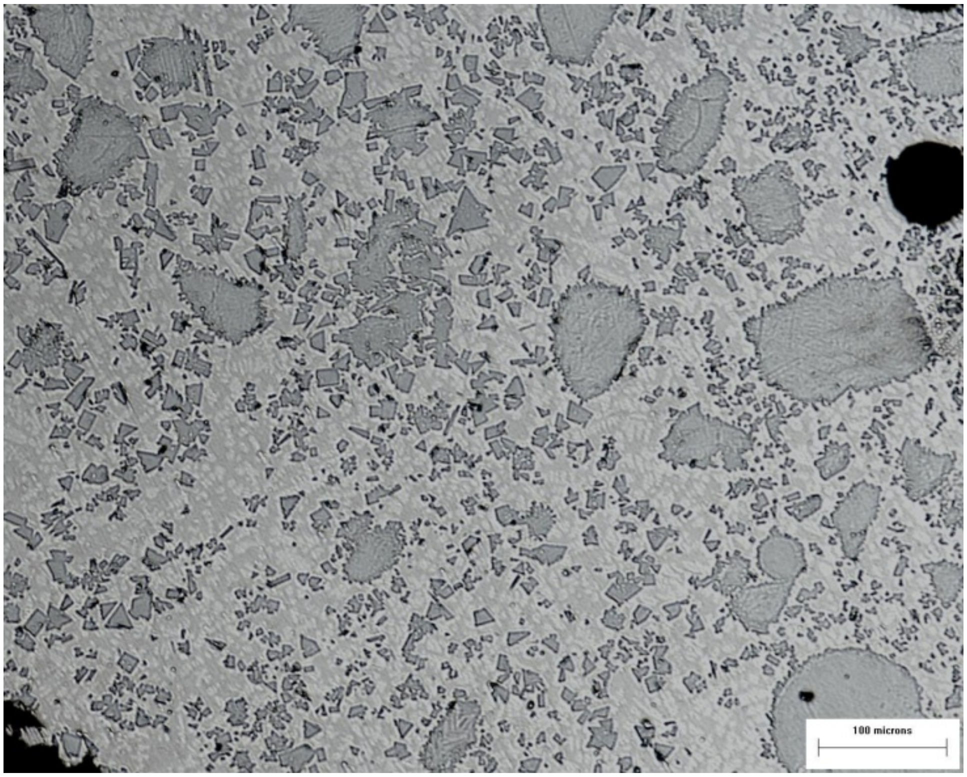

(c)

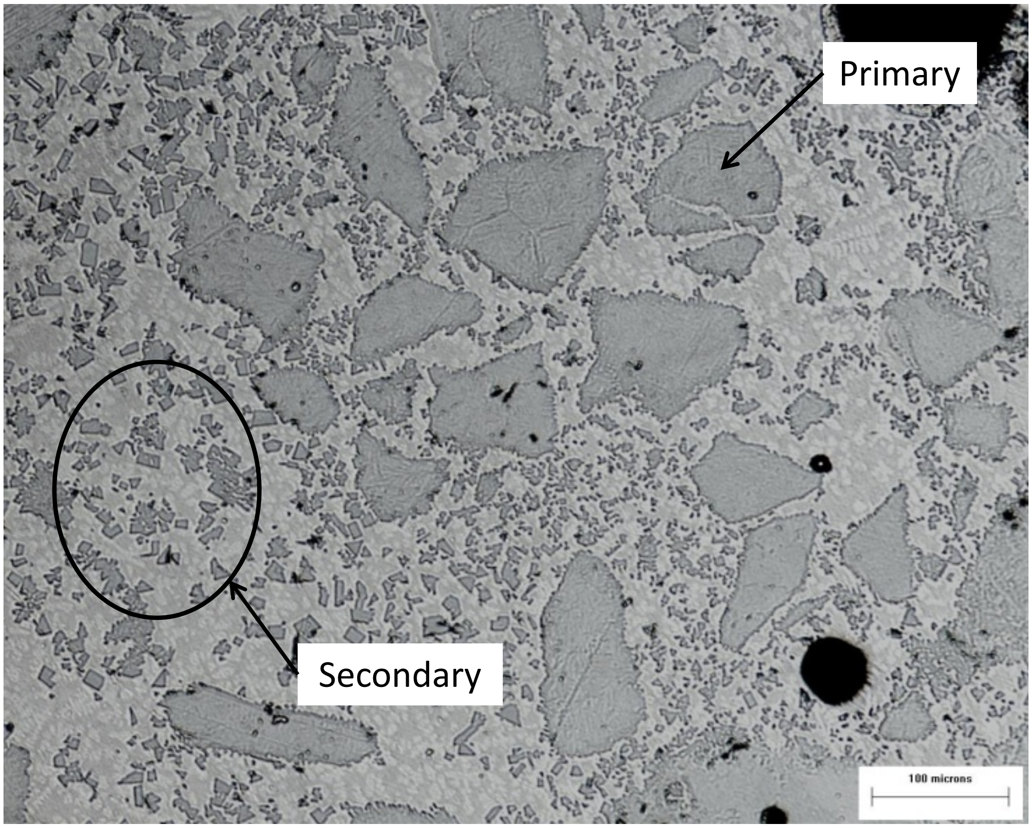

(d)

Figure 5.7 Microstructures of overlay deposits. (a) and (b) are overlay deposits using the machine settings as where the minimum heat content was discovered (194 A). (c) and (d) were deposited using higher welding current (213 A). Primary and secondary carbides are shown in (d).

Figure 5.5 shows the bead appearance after deposition of the overlay. The bead shape is non-uniform and non-symmetric and there are substantial carbon deposits on either side of the weld bead. The shielding gas used was pure argon, which could be part of the reason for the erratic deposit. Using a non-oxidizing gas inhibits the formation of oxides on the surface of the substrate that act as preferential emitters of electrons. This increases the mobility of the cathode spot and leads to irregular deposits.

By visual inspection the overlay generated by the parameters that resulted in minimum droplet heat content showed higher primary carbide survival. In Figure 5.5 (a) and (b), the majority of carbides that survived are large primary carbides or primary carbides that have been partially dissolved. Small, polygonal secondary carbides exist in both cases, but more extensively in (c) and (d) indicating that higher heat input led to more dissolution and recrystallization of secondary carbides.

Large porosities are seen in overlays produced by both parameters. It is possible that this is due to atmosphere being present in the core of the wire. Oxygen and nitrogen decompose into ions and electrons as they are introduced to the plasma. The solubility of these ions in molten nickel is very high; as such, some oxygen and nitrogen go into solution in the melt. When cooled, the solubility drops considerably. The oxygen and nitrogen condense into gases that cannot escape the solidifying metal.

Chapter 6 : Conclusions and Recommendations

Conclusions

- A solid state calorimeter that accounts for thermal gradients was developed for the purpose of measuring droplet heat content in free-flight GMAW. The calorimeter measured droplet heat content and temperature for ER70S-6 steel wire that agreed with previous studies and indicated a minimum droplet temperature in the transition from globular to spray transfer.
- Droplet heat content reached a minimum in 1.6 mm Ni/WC tubular consumables shielded with argon at approximately 190 A. The minimum occurred within the broad transition from globular to spray transfer. Approximate droplet temperature was 2800 K. Droplet heat content ranged from 1300 to 1500 J/g.
- Arc behavior with Ni/WC wires was erratic and unpredictable. This behavior led to unpredictable metal transfer and mixed transfer modes, especially when operating in welding currents below ~194 A.
- Measured droplet heat content was consistent with two modeling approaches.

Recommendations

Overlay deposition using GMAW has a bright future, but work should go into key areas to further develop and tailor processes and consumables for ideal overlays.

- Arc stabilization is critical to producing quality overlays. If the arc is stabilized, detachment events would become more predictable and pulsing could become feasible.

- The nickel sheaths of the Ni/WC wires are very stiff and difficult to feed through a traditional “push” type wire feeder. A “pull” type or “push/pull” type system should be used to avoid kinking and jams.
- There are several wire manufacturers who use different sheath thicknesses and alloy additions. These changes lead to different behavior and resulting weld microstructure. Although costly, the end user should develop a custom wire tailored to their needs to consistently achieve the desired result.
- This study focused only on electrode positive polarity. Reversing the polarity has been shown to decrease droplet temperature [18], but also increase instability of the arc. It may be possible to create a situation in which the WC powders act as a thermionic emitter to help stabilize the arc in electrode negative polarity.
- Low ionization potential elements such as potassium could be added in small quantities to stabilize the arc in electrode positive and electrode negative polarities [52]. This may aid in the predictability of metal transfer as well as making pulsing a possibility.
- The polynomial approximation of thermal gradients in this study allow for calculation of early and late stage thermal gradients that develop within the calorimeter. Late stage thermal gradients can be used to quantify the heat loss and further improve the accuracy of the calorimeter.
- It is possible that the addition of nitrogen getters, such as aluminum, could be added to the core to help reduce porosity on the final overlay.

References

1. Ruwanpura, J. and G. Jergeas, *Why Cost and Schedule Overruns on Mega Oil Sands Projects?* Cost Engineering, 2010. **51**(1): p. 24-27.

2. Moritis, G., *Continued Alberta Oil Sands Production Growth Seen.* Oil & Gas Journal, 2010. **108**(25): p. 42-46.

3. Neville, A., et al., *Assessing metal matrix composites for corrosion and erosion-corrosion applications in the oil sands industry.* Corrosion, 2006. **62**(8): p. 657-675.

4. Deuis, R.L., J.M. Yellup, and C. Subramanian, *Metal-matrix composite coatings by PTA surfacing.* Composites Science and Technology, 1998. **58**(2): p. 299-309.

5. Flores, J.F., et al., *An experimental study of the erosion–corrosion behavior of plasma transferred arc MMCs.* Wear, 2009: p. 213-222.

6. Mendez, P.F., N.T. Jenkins, and T.W. Eagar. *Effect of Electrode Droplet Size on Evaporation and Fume Generation in GMAW*. in *Gas Metal Arc Welding for the 21st Century*. 2000. Orlando, FL: American Welding Society.

7. Jenkins, N.T., P.F. Mendez, and T.W. Eagar. *Effect of Arc Welding Electrode Temperature on Vapor and Fume Composition*. in *Trends in Welding Research*. 2005. Pine Mountain, GA.

8. Badisch, E. and M. Kirchgaßner, *Influence of welding parameters on microstructure and wear behaviour of a typical NiCrBSi hardfacing alloy reinforced with tungsten carbide.* Surface & Coatings Technology, 2008: p. 6016-6022.

9. Klimpel, A., et al., *Abrasion resistance of GMA metal cored wires surfaced deposits.* Journal of Materials Processing Technology, 2005. **164**: p. 1056-1061.

10. Klimpel, A., et al., *The study of properties of Ni-WC wires surfaced deposits.* Journal of Materials Processing Technology, 2005. **164**: p. 1046-1055.

11. Choi, L., et al. *Effect of Welding Parameters on Tungsten Carbide - Metal Matrix Composites Produced by GMAW* in *Canadian Welding Association Annual Conference*. 2011. Banff, AB.

12. Ma, J. and R.L. Apps, *MIG Transfer Discovery of Importance to Industry*. Welding and Metal Fabrication, 1982. **50**(7): p. 307-316.

13. Soderstrom, E.J., K.M. Scott, and P.F. Mendez, *Calorimetric Measurement of Droplet Temperature in GMAW.* Welding Journal, 2011. **90**(4): p. 1s-8s.

14. Villeminot, P., *Argon MIG Welding of Mild Steel, Thermal Study of the Stick-Out, Transfer Temperature. (In French).* Conference Proceedings of *Soud. Techn. Conn.*, 1967. **21**(9-10): p. 367-380.

15. Lu, M.J. and S. Kou, *Power Inputs in Gas Metal Arc Welding of aluminum - Part 1.* Welding Journal, 1989: p. 382s-388s.

16. Jelmorini, G., G.W. Tichelaar, and G.J.P.M.v.d. Heuvel, *Droplet Temperature Measurements in Arc Welding.* IIW Doc. 212-411-77 International Institute of Welding, London, England, 1977.

17. Guest, S.D., *Personal communication*. December 2010.

18. Pokhodnya, I.K. and A.M. Suptel, *Heat Contents of Droplets of Electrode Metal in Gas Shielded Arc Welding.* Automatic Welding Ussr, 1967. **20**(2): p. 16-24.

19. Pokhodnya, I.K. and A.M. Suptel, *Heat Content of Droplets of Electrode Metal in CO2 Welding.* Automatic Welding Ussr, 1970. **23**(10): p. 5-10.

20. Ando, K. and K. Nishiguchi, *Mechanism of Formation of Pencil-Point-Like Wire Tip in MIG Arc Welding* IIW Doc. 212-156-68, 1968: p. 1-10.

21. Ozawa, M. and T. Morita, *The Measurement of Heat Quantity in Melted Metals.* Journal of the Japan Welding Society, 1963. **32**(2): p. 52-59.

22. Heiro, H. and T.H. North, *The Influence of Welding Parameters on Droplet Temperature During Pulsed Arc Welding.* Welding and Metal Fabrication, 1976. **44**(9): p. 482-485, 518.

23. Fu, X.-S., M. Ushio, and F. Matsuda, *Melting Characteristics of Some Steel and Aluminum Alloy Wires in GMA Welding.* Transactions of JWRI, 1983. **12**(2): p. 7-13.

24. Lu, M.J. and S. Kou, *Power Inputs in Gas Metal Arc Welding of Aluminum - Part 2.* Welding Journal, 1989: p. 452s-456s.

25. Soderstrom, E., *Gas Metal Arc Welding Electrode Heat and Mass Transfer Mechanisms*, in *Metallurgical and Materials Engineering*, P.F. Mendez, Editor. 2009, Colorado School of Mines: Golden, CO.

26. Mills, K.C., *Recommended values of thermophysical properties for selected commercial alloys*. 2002, Cambridge: Woodhead. ix, 244.

27. McBride, B.J., S. Gordon, and M.A. Reno, *NASA Technical Paper 3287.* 2001.

28. White, G.K. and S.J. Collocott, *Heat Capacity of Reference Materials: Cu and W.* J. Phys. Chem. Ref. Data, 1984. **13**(4): p. 1251.

29. Stephens, R. and J. Boerio-Goates, *Heat Capacity of Copper on the ITS-90 Temperature Scale Using Adiabatic Calorimetry*. J. Chem. Thermodynamics, 2004. **36**: p. 857-863.

30. Tsotsas, E. and H. Martin, *Thermal Conductivity of Packed Beds: A Review*. Chem. Eng. Process., 1987. **22**: p. 19-37.

31. Ozaki, Y. and R.H. Zee, *Investigation of thermal and hydrogen effects on emissivity of refractory metals and carbides.* Materials Science and Engineering, 1995. **A202**: p. 134-141.

32. Seetharaman, S., ed. *Fundamentals of Metallurgy*. 2005, Woodhead Publishing Limited: Cambridge.

33. Krivtsun, I., et al. *Model of Heat-, Mass- and Charge Transfer in Welding Arc Column and Anode Region*. in *9th International Seminar of Numerical Analysis of Weldability*. 2009. Graz-Seggau, Austria.

34. Waszink, J.H. and G.J.P.M. Van den Heuvel, *Heat Generation and Heat Flow in the Filler Metal in GMA Welding.* Welding Journal, 1982: p. 269s-282s.

35. Nemchinsky, V.A., *Plasma Parameters Near a Small Anode in a High-Pressure Arc (Gas Metal Arc Welding).* Journal of Physics D: Applied Physics, 1994. **27**: p. 2515-2521.

36. Sanders, N.A. and E. Pfender, *Measurement of anode falls and anode heat transfer in atmospheric pressure high intensity arcs.* J. Appl. Phys., 1984. **55**(3): p. 714-722.

37. Lancaster, J.F., *The Physics of Welding*. 2nd ed. 1986, Elmsfod, NY: Pergamon Press. 341.

38. Heberlein, J., J. Mentel, and E. Pfender, *The Anode Region of Electric Arcs: A Survey.* J. Phys. D: Appl. Phys., 2010. **43**.

39. Lehnhoff, G. and P. Mendez, *Scaling of non-linear effects in heat transfer of a continuously fed melting wire.* International Journal of Heat and Mass Transfer, 2011. **54**: p. 2651-2660.

40. Haidar, J., *An Analysis of Heat Transfer and Fume Production in Gas Metal Arc Welding. III.* Journal of Applied Physics, 1999. **85**(7): p. 3448-3459.

41. Deam, R., S.W. Simpson, and J. Haidar, *A Semi-Empirical Model of the Fume Formation from Gas Metal Arc Welding.* Journal of Physics D: Applied Physics, 2000. **33**: p. 1393-1402.

42. Kogan, M.N. and N.K. Makashev, *Role of the Knudsen layer in the theory of heterogeneous reactions and in flows with surface reactions* Fluid Dynamics, 1971. **6**(6): p. 913-920.

43. Haidar, J. and J.J. Lowke, *Predictions of metal droplet formation in arc welding.* J. Phys. D: Appl. Phys., 1996. **29**: p. 2951-2960.

44. Hu, J. and H.L. Tsai, *Metal Transfer and Arc Plasma in Gas Metal Arc Welding.* Journal of Heat Transfer, 2007. **129**(8): p. 1025-1034.

45. Hu, J. and H.L. Tsai, *Heat and mass transfer in gas metal arc welding. Part II: The metal.* International Journal of Heat and Mass Transfer, 2007. **50**(5-6): p. 808-820.

46. Watanabe, H., et al., *Phase (Liquid/Solid) Dependence of the Normal Spectral Emissivity for Iron, Cobalt, and Nickel at Melting Points.* International Journal of Thermophysics, 2003. **24**(2): p. 473-488.

47. Kurskov, A.A., et al., *An Approximate Method For Measurement of the Spectral Distribution of the Emissivity in Inhomogeneous Plasma.* Journal of Applied Specroscopy, 1994. **60**(3-4): p. 297-301.

48. Rosenhow, W.M. and J.P. Hartnett, *Handbook of Heat Transfer*, ed. M. Hill. 1973, New York, NY. 8-126.

49. Waszink, J.H. and M.J. Piena, *Experimental Investigation of Drop Detachment and Drop Velocity in GMAW.* Welding Journal, 1986: p. 289s-298s.

50. Haidar, J., *The dynamic effects of metal vapour in gas metal arc welding.* J. Phys. D: Appl. Phys., 2010. **43**: p. 11.

51. Schnick, M., et al., *Metal vapour causes a central minimum in arc temperature in gas–metal arc welding through increased radiative emission.* J. Phys. D: Appl. Phys., 2010. **43**: p. 5.

52. Lesnewich, A., *Electrode Activation for Inert-Gas-Shielded Metal-Arc Welding.* Welding Journal, 1955. **35**(12): p. 1167-1178.

53. Mendez, P.F. and E.J. Soderstrom, *Gas metal arc welding methods and aparatus*. United States Patent Application # 2006/0237411 A1. .

54. Soderstrom, E., *Influence of Ar-Co2 Mixtures and Thin Electrodes on Metal Transfer in Gas Metal Arc Welding*, in *Metallurgical and Materials Engineering*, P.F. Mendez, Editor. 2007, Colorado School of Mines: Golden, CO.

55. Matula, R.A., J. Phys. Chem. Ref. Data, 1979. **8**(4): p. 1147.

56. Levinson, L.S., *High-Temperature Heat Content of Tungsten Carbide and Hafnium Carbide*. The Journal of Chemical Physics, 1964. **40**(5): p. 1437-1438.

57. Andon, R.J.L., J.F. Martin, and K.C.Mills, *Heat Capacity and Entropy of Tungsten Carbide*. J. Chem. Thermodynamics, 1975(7): p. 1079-1084.

58. Reeber, R.R. and K. Wang, *Thermophysical Properties of alpha-Tungsten Carbide*. J. Am. Ceram. Soc., 1999. **82**(1): p. 129-135.

59. Emelyanov, A.E., *High Temperatures-High Pressures*. 1994. **26**: p. 663.

Appendix A: Welding Equipment

The equipment used in this study is commercially available and typical of the equipment that is used heavily in industry. An important aspect of this project was being able to replicate results in the field or in a shop; therefore, it was necessary to choose equipment that could be easily duplicated in a different location. A schematic representation of the experimental setup is shown in Figure A.1, while a view of how the setup looks in the lab is shown in Figure A.2.

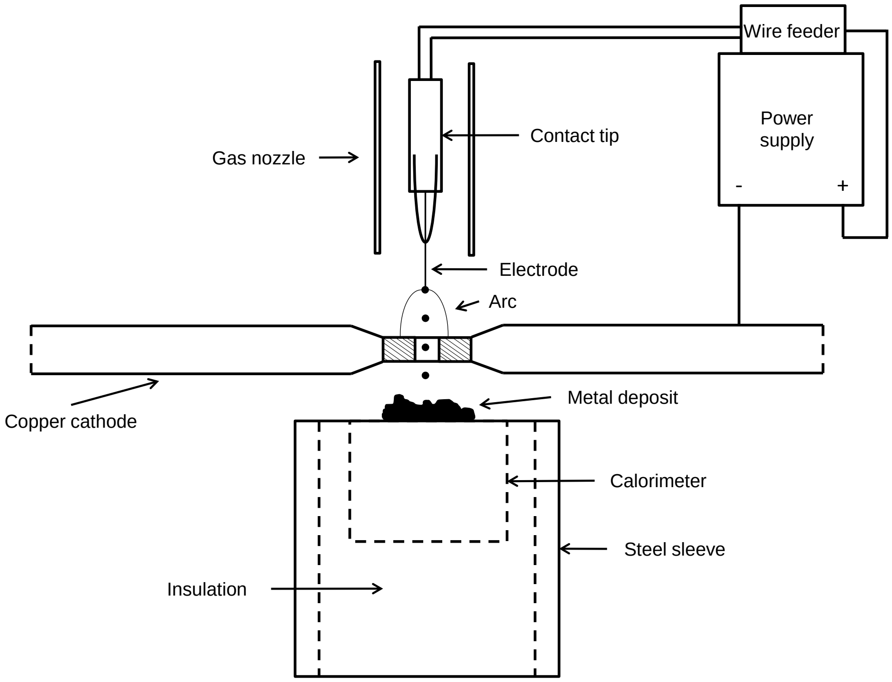

Figure A.1 Schematic representation of the equipment used for this study.

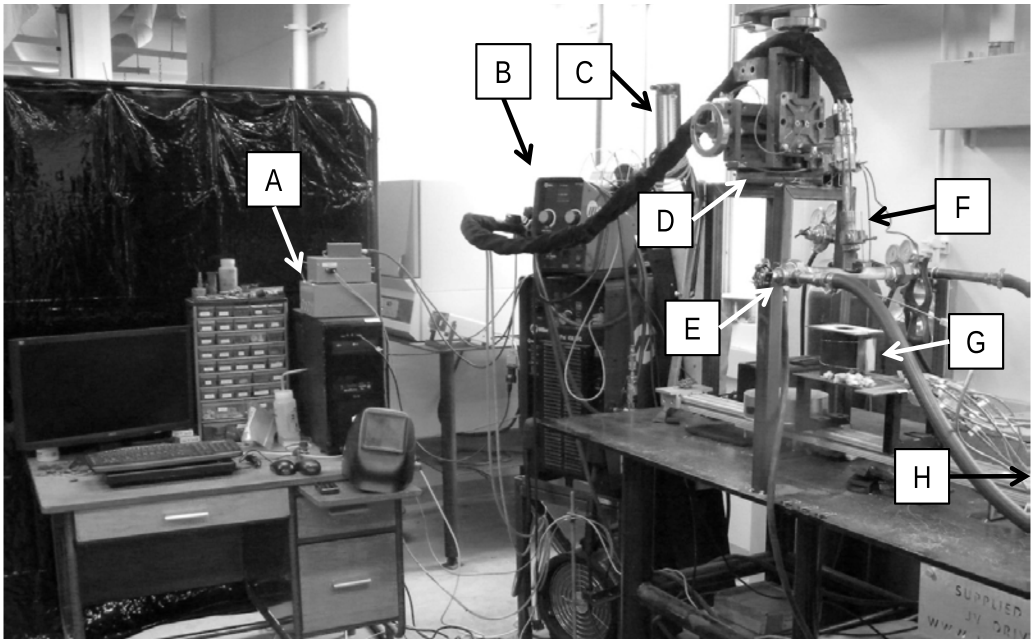

A) Data Acquisition System
B) Power Supply/Wire Feeder
C) Gas Rotameter
D) X-Y-Z Positioner
E) Copper Cathode
F) Welding Torch
G) Calorimeter
H) Water Tank (Out of picture)

Figure A.2 View of the apparatus as it sits in the lab.

Power Supply

The power supply used was a Miller PipePro 450RFC operated in constant potential mode.

Wire Feeder

The wire feeder used was a PipePro Single Feeder interfaced directly to the PipePro 450 RFC power supply. Knurled drive rolls were used to minimize the pressure needed to feed the stiff Ni/WC wire and to prevent kinking while the wire was fed through the torch.

Welding Torch

The welding torch used was a Tregaskiss Tough Gun I.C.E.® water-cooled robotic MIG torch. Although the torch has the capability to be coupled to a robotic arm, no automation was used in this study.

Shielding gas

To prevent excess oxidation to the copper cathode commercially pure argon was used as the shielding gas in each trial instead of the recommended Ar/O_2 mixture. The shielding gas was metered through an Omega model FL-2GP-40ST-40ST rotameter to precisely control gas flow. Flow rate was set to 35 SCFH and maintained throughout the study.

Contact Tip

An important consideration when studying GMAW is the contact tip. A traditional copper contact tip offers a contact point and conduit through which the wire is delivered to the arc. The typical design, however, presents a problem when trying to control the contact point because there is no way to determine or control where the wire makes contact. The contact tips used in this study are 35 mm (1.375 in.) in length, leading to an uncertainty in electrode extension of up to 35 mm. Although practically the uncertainty is smaller, it is not negligible. The extra Joule heating imposed on the wire would be large enough to significantly affect resulting droplet temperatures and transfer modes. A different contact tip design was required to better control the contact point.

Soderstom [53, 54] developed a novel contact tip that enabled his study of GMAW with thin electrodes. The “U-wire” contact tip shown in Figure A.3 allows for precise control of the contact point by forcing the electrode to make contact with the U-wire. Although there may be more than one contact point, the current density in the wire between the first contact point and the U-wire is negligible as shown in a subsequent calculation.

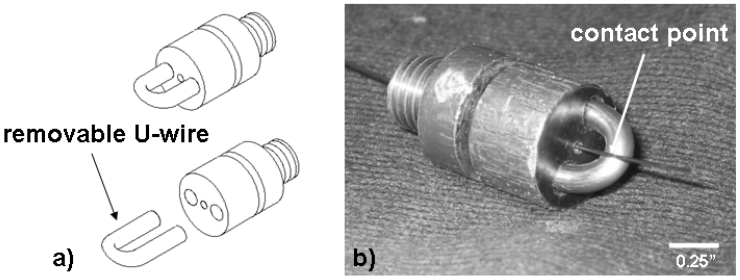

Figure A.3 "U-wire" contact tip designed by Soderstrom. This design eliminates the uncertainty involved with the contact point of the wire.

The method used by Soderstrom to manufacture these tips was timely and tedious [54], and resulted in a sacrificial anode that was not needed in the current study. A similar contact tip was developed and used. The new design is a standard contact tip with a U-wire welded to the side, shown in Figure A.4. This “Bend-back” contact tip was easy to manufacture, reliable, reusable and allowed for precise control of the wire contact point.

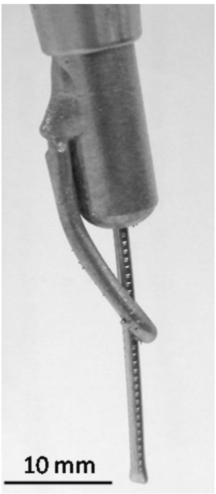

Figure A.4 "Bend-back" type contact tip used in this study.

The “Bend back” type contact tip allows for the precise control of the contact point, but introduces a situation in which the electrode and contact tip act as parallel resistors between the U-wire and body of the main contact tip. The maximum distance this configuration could exist is approximately 48 mm (1.875 in.). Therefore, this length was assumed for calculating resistance in the following calculation. The contact tip and wire can be represented as parallel resistors by:

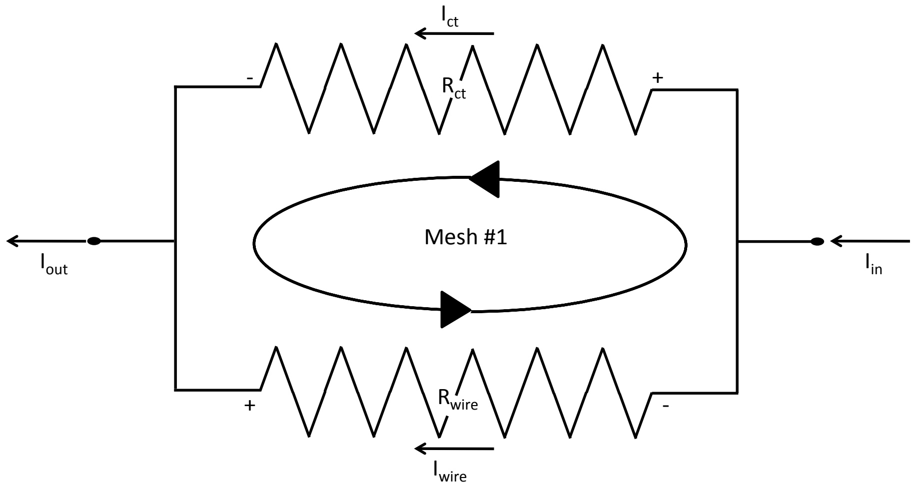

Figure A.5 Schematic of the equivalent electrical diagram of the wire and contact tip configuration.

where the sum of the voltages about Mesh #1 equates to zero:

$$\sum V_{Mesh\ \#1} = 0$$

Equation A.1

Therefore:

$$(R_{ct})(I_{ct}) + (R_{wire})(I_{wire}) = 0$$

Equation A.2

And:

$$I_{ct} = I_{in} - I_{wire}$$

Equation A.3

Therefore:

$$I_{wire} = \frac{-(R_{ct})(I_{in})}{R_w - R_{ct}}$$

Equation A.4

The overall resistance of the contact tip or wire is given by:

$$R = \frac{\rho_o l}{A}$$

Equation A.5

where ρ_o is the electrical resistivity, l is the length and A is the cross sectional area of the wire or contact tip. Approximating the resistance of the wire and contact tip using room temperature properties yields equations B.6 and B.7. Room temperature resistivity data for copper taken from [55].

$$R_{wire} = \frac{\rho_{o,wire} l_{wire}}{A_{wire}} = \frac{(2.18 \times 10^{-07})(0.048)}{1.96 \times 10^{-06}} = 0.005\ \Omega$$

Equation A.6

$$R_{ct} = \frac{\rho_{o,ct} l_{ct}}{A_{ct}} = \frac{(1.722 \times 10^{-08})(0.048)}{4.91 \times 10^{-06}} = 1.7 \times 10^{-04}\ \Omega$$

Equation A.7

plugging into equation B.4 leaves:

$$I_{wire} = \frac{-(R_{ct})(I_{in})}{R_w - R_{ct}} = \frac{-(1.7 \times 10^{-04})(I_{in})}{0.005 - 1.7 \times 10^{-04}}$$

$$I_{wire} = -0.035 I_{in}$$

Equation A.8

The negative is indicative of the method used to solve Equation A.1 and does not imply the current is traveling in the opposite direction. Using this relationship, at 200 A welding current 193 A would flow through the contact tip and 7 A would flow through the wire. The amount of Joule heating the wire would see in this region is negligible compared to the Joule heat gained in the electrode extension region.

Data Acquisition

Recording thermocouple readings and current/voltage output of the power supply was critical to the analysis of droplet temperature. The data acquisition rate, however, could not be the same for both data sets. Because the power supply is operated in constant potential mode, it uses the voltage signal to control the welding current to keep the welding voltage, and therefore arc length, relatively constant. These changes happen within a matter of tenths of milliseconds. Therefore, a data acquisition rate of 10,000 Hz was used to monitor the current/voltage signals. On the contrary, temperature changes in the calorimeter happen much slower and do not require fast data acquisition rates. 10 Hz was used for acquiring temperature data.

Two different data acquisition rates cannot be captured on the same board; therefore, it was necessary to use two systems. Current was monitored using an LEM model HTA 600S current transducer while voltage was monitored using an LEM model LV 25-P voltage transducer. The transducer outputs were connected to a Data Translation model DT740 screw panel and model DT3010 PCI data acquisition card. A LabView program written specifically for this work was used to acquire the data and save the text file for further analysis in Matlab using a program written by Soderstrom [25]. This software allowed for computing average welding current and welding voltage, along with calculating a Fast Fourier Transform to approximate the droplet detachment frequency.

K-type thermocouples were monitored by an Omega model OMB-DAQ-3001 USB board connected to an OMB-PDQ30 expansion module. DaqView software was used to acquire temperature data and create the text files that were analyzed in Matlab. The program written specifically for the solid state calorimeter compiles the data from each thermocouple, applies a calibration curve, solves Equation 2.6 and returns the total droplet heat content and/or average droplet temperature. In addition, it has the ability to calculate the temperature gradients that are present in the calorimeter in any axes at any time. The code is included in Appendix F.

Noise Reduction in Thermocouples

Initial connection of the thermocouples to the data acquisition board resulted in significant interference during the time when the arc was engaged, as shown in Figure A.6.

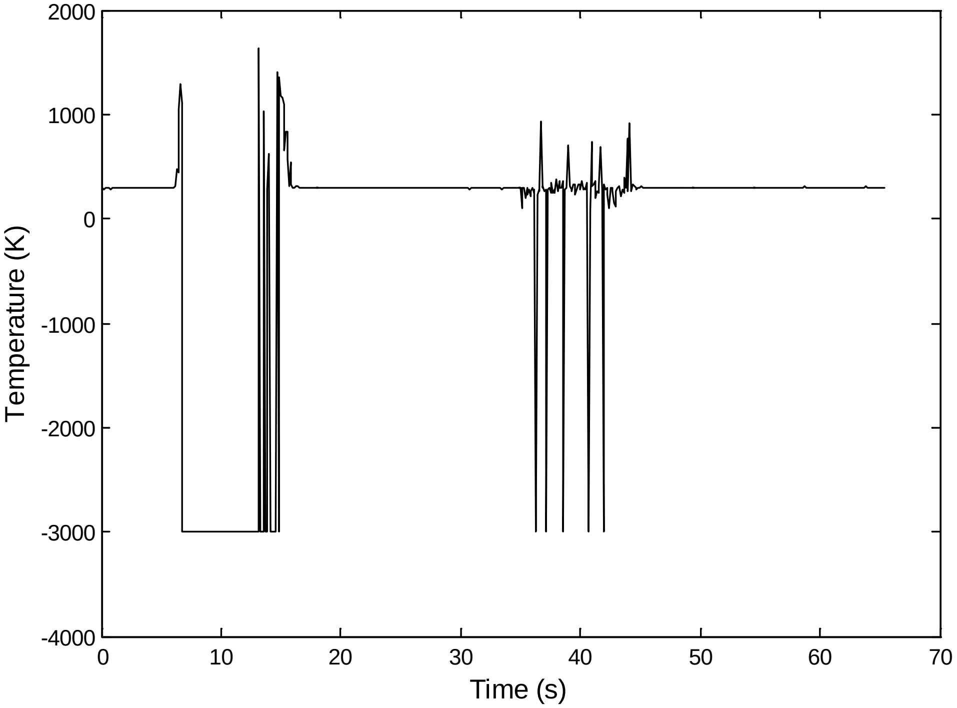

Figure A.6 Temperature vs. time plot while the arc is engaged. The points in which the arc was active are marked with drastic changes in the thermocouple temperature readings.

While the arc was engaged, significant electromagnetic fields were generated near the welding cables, torch and arc. The magnetic fields induce voltages within the thermocouples to significantly alter the readout. Due to the proximity of the thermocouples to the arc, it was necessary to shield the leads of the thermocouples from the interference. Low-noise thermocouples, Omega model number GKQSS-116U-12, equipped with a grounding strap coupled to shielded extension wire reduced the noise significantly, but not completely. In addition, it was necessary to oversample the input data by a factor of 4096. An example of the conditioned thermocouple output is shown in Figure A.7.

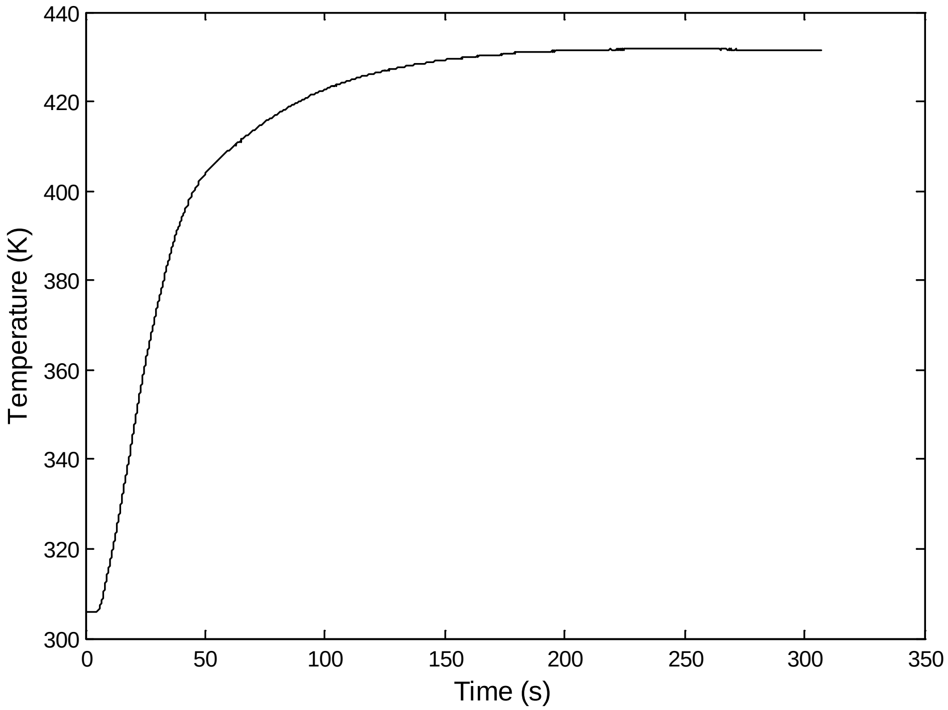

Figure A.7 Conditioned thermocouple output. The example is a single thermocouple in the calorimeter while depositing steel.

Appendix B: Calorimeter Design and Schematic

In the initial stages of the solid-state calorimeter design it was necessary to approximate the energy that would be added to the calorimeter to obtain realistic dimensions. At the beginning of the study, it was determined that the calorimeter would be cylindrical for two reasons. First, a cylindrical shape would offer adequate heat transfer geometry. Also, cylcinders of high purity copper are readily available and relatively inexpensive. The following analysis shows the methodology of developing the dimensions of the calorimeter. The design stage was conducted before the H.C. Starck wire was chosen as the test wire, so the values given in Table A.1 are estimated.

Table B.1 Properties for estimating droplet enthalpy change. Volume fractions of WC/W_2C are assumed.

Property	*Symbol*	*Unit*	*Value*
Density of Ni [26]	ρ_{Ni}	g/cc	8.9
Density of WC/W_2C	$\rho_{WC/W2C}$	g/cc	16.5
Ni volume fraction	f_{Ni}	-	0.50
WC/W_2C volume fraction	$f_{WC/W2C}$	-	0.50
Volume deposited	$V_{droplets}$	cc	3.5
Mass of Ni deposited	m_{Ni}	g	15.6
Mass of WC/W_2C deposited	$m_{WC/W2C}$	g	28.9
Melting temp. of Ni [26]	$T_{m,Ni}$	K	1728
Final droplet temp.	T_f	K	465
Initial droplet temperature	T_i	K	2600
Estimated droplet enthalpy change	ΔH	J	43,109
Weber number of falling droplet	W_e	-	30

Based on the estimation of the amount of Ni and WC/W_2C present in the deposit and initial temperature of the droplets an estimated droplet enthalpy change was established. Assuming all of the energy from the droplets was transferred to the calorimeter, the estimated droplet enthalpy change is also the change of enthelpy in the calorimeter. In Table A.2 the calorimeter enthalpy change is related to the thermophysical properties of copper to establish the volume of copper required to achieve the estimated temeprature change of 165 K.

Table B.2 Properties used for establishing the dimensions of the cylindrical calorimeter.

	Symbol	*Unit*	*Value*
Enthalpy change of Cu	ΔH	J	43,109
Specific heat capacity of Cu	c_p	J/gK	0.4133
Density of Cu	ρ_{Cu}	g/cc	8.93
Initial temp. Cu	$T_{i, Cu}$	K	298
Final temp. Cu	$T_{f, Cu}$	K	465
Mass of Cu needed for energy balance	m_{Cu}	g	625
Volume of Cu	V_{Cu}	m^3	70
Cylinder diameter	d	cm	5.08
Cylinder height	h	cm	3.5

The results of this analysis indicate the final dimensions of the calorimeter to achieve a temperature change of 165 K if 3.5 cc of Ni/WC at 2600 K is deposited on the surface. In Table B.1 the Weber number of the falling droplets was calculated to approximate whether the droplets would “bounce” when they struck the surface or if they would “splash.” The calculated value of 30 indicates the latter, which is the ideal case for this study.

A schematic of the calorimeter is shown in Figure B.1 with the thermocouple positions given in Table B.3.

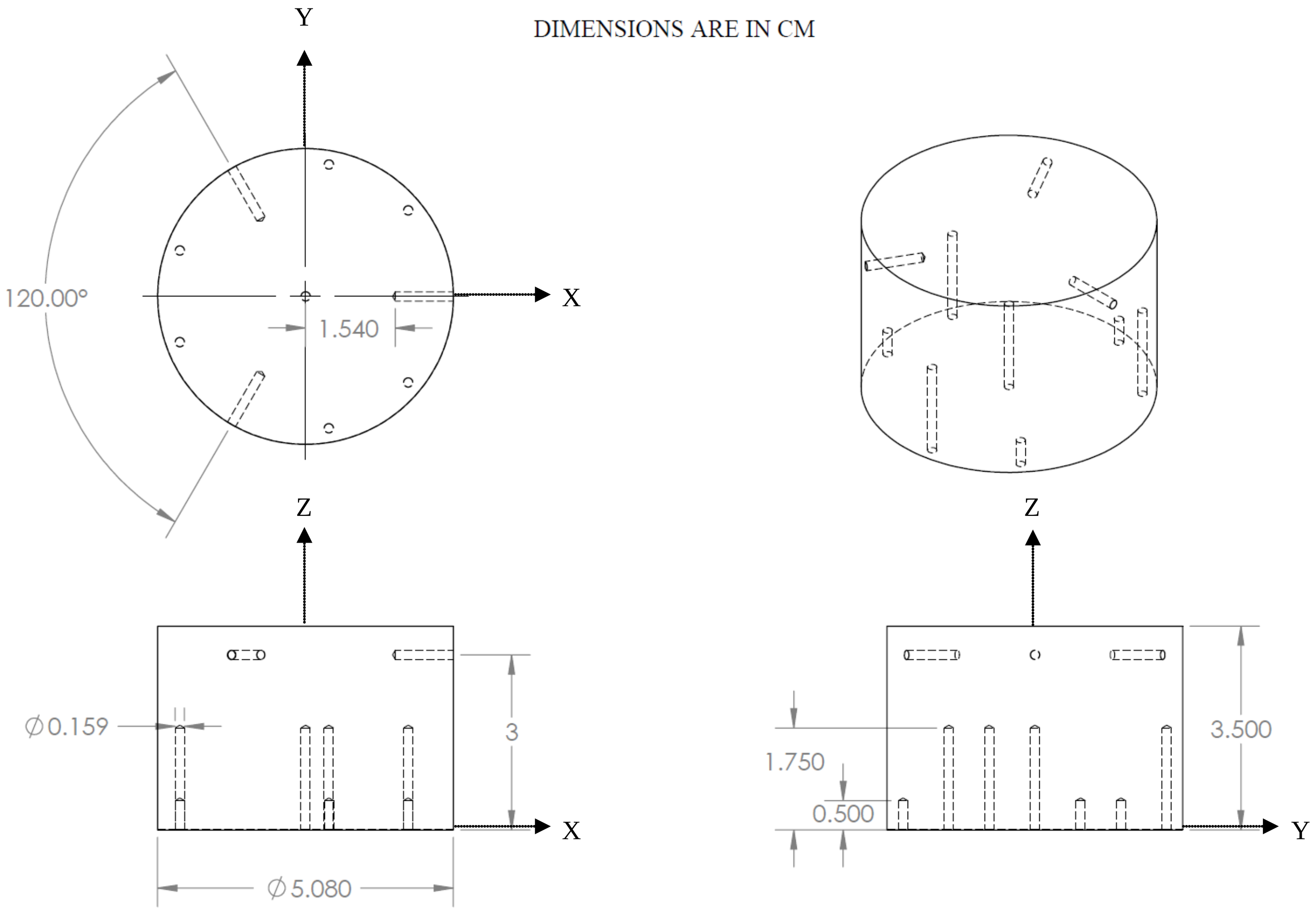

Figure B.1 Mechanical drawing of the solid-state calorimeter.

Table B.3 Thermocouple positions from the origin, located on the centerline on the bottom plane.

	Location on Axis (cm)		
TC #	X	Y	Z
1	0	0	1.75
2	1.54	0	3.0
3	1.76	-1.48	1.75
4	0.4	-2.27	0.5
5	-0.77	-1.33	3.0
6	-2.16	-0.79	1.75
7	-2.16	0.79	0.5
8	-0.77	1.33	3.0
9	0.4	2.27	1.75
10	1.76	1.48	0.5

Appendix C: Calorimeter Integrations

Each h_i function presented in Equations 2.1 and 2.2 had to be integrated over the volume of the calorimeter to account for the enthalpy of the entire body. The dimensionless h_i function is represented by:

$$\begin{aligned} h_i = {} & c_{i,1} + c_{i,2}x + c_{i,3}y + c_{i,4}z + c_{i,5}xy + c_{i,6}xz + c_{i,7}yz + c_{i,8}x^2 + c_{i,9}y^2 \\ & + c_{i,10}z^2 \end{aligned}$$

Equation C.1

h_i expressed in cylindrical coordinates:

$$\begin{aligned} \iiint\limits_V h_i dV = \iiint\limits_{0\,0\,0}^{H\,R\,2\pi} & (c_{i,1} + c_{i,2}r\cos\theta + c_{i,3}r\sin\theta + c_{i,4}z + c_{i,5}r^2\cos\theta\sin\theta \\ & + c_{i,6}r\cos\theta\, z + c_{i,7}r\sin\theta\, z + c_{i,8}r^2\cos^2\theta + c_{i,9}r^2\sin^2\theta \\ & + c_{i,10}z^2)\, dzdrrd\theta \end{aligned}$$

Equation C.2

Integration over the volume of the cylinder yields:

$$\begin{aligned} v_i = c_{i,1}[V] + c_{i,2}[r\sin 2\pi - r\sin 0] + c_{i,3}\left[-\frac{1}{3}HR^3(\cos 2\pi - \cos 0)\right] \\ + c_{i,4}\left[\frac{2\pi H^2R^2}{4}\right] + c_{i,5}\left[\frac{HR^4}{8}(\sin^2 2\pi - \sin^2 0\right] \\ + c_{i,6}\left[\frac{H^2R^3}{6}(\sin 2\pi - \sin 0)\right] + c_{i,7}\left[\frac{H^2R^3}{6}(\cos 2\pi - \cos 0)\right] \\ + c_{i,8}\left[\frac{HR^4\pi}{4}\right] + c_{i,9}\left[\frac{HR^4\pi}{4}\right] + c_{i,10}\left[\frac{H^3R^22\pi}{6}\right] \end{aligned}$$

Equation C.3

Leaving five non-zero terms and the final equation for v_i:

$$v_i = c_{i,1}V + c_{i,4}\left[\frac{2\pi H^2 R^2}{4}\right] + c_{i,8}\left[\frac{HR^4\pi}{4}\right] + c_{i,9}\left[\frac{HR^4\pi}{4}\right] + c_{i,10}\left[\frac{H^3R^2 2\pi}{6}\right]$$

Equation C.4

Appendix D: Calorimeter Calibration

Table D.1 Calorimeter calibration results using one source for copper enthalpy tabulation. % discrepancy in enthalpy is highlighted.

Test no.	$T_{cal,initial}$	$T_{sn,initial\ TC}$	$T_{sn,initial\ calc}$ *(K)*	*% diff*	m_{sn} *(g)*
20101118004	351.60	556.0	559.20	0.41	34.66
20101119001	295.20	654.20	683.00	4.40	32.82
20101119002	311.70	585.22	600.30	2.58	35.24
20101119003	332.30	645.50	655.70	1.58	39.71
20101119004	336.70	577.70	583.90	1.07	17.55
20101130001	417.80	680.30	653.60	-3.92	34.83
20101130002	393.80	647.80	631.90	-2.45	32.37
20101130003	468.70	725.80	661.90	-8.80	16.55
20102230004	453.10	686.50	623.30	-9.21	33.86

Test no.	$T_{sn,final}$ *(K)*	ΔT *(K)*	$H_{cal,\ tot}$ *(J)*	H_{Sn}	*% diff*
20101118004	366.20	14.60	3749	3730	0.51
20101119001	314.40	19.20	4916	4691	4.80
20101119002	329.00	17.30	4466	4340	2.90
20101119003	353.00	20.70	5333	5236	1.85
20101119004	344.70	8.00	2091	2066	1.21
20101130001	433.10	15.30	3982	4208	-5.37
20101130002	408.40	14.60	3732	3855	-3.19
20101130003	475.40	6.70	1748	2000	-12.60
20102230004	466.20	13.10	3345	3854	-13.21

Table D.2 Calorimeter calibration results after the calibration function was applied. These results were obtained using average copper enthalpy. % discrepancy in enthalpy is highlighted.

Test no.	$T_{cal,initial}$	$T_{sn,initial\ TC}$	$T_{sn,initial\ calc}$ *(K)*	*% diff*	m_{sn} *(g)*
20101118004	351.60	556.90	559.6	0.48	34.66
20101119001	295.20	654.20	650.6	-0.55	32.82
20101119002	311.70	585.22	580.9	-0.74	35.24
20101119003	332.30	645.50	648.7	0.50	39.71
20101119004	336.70	577.70	573.5	-0.73	17.55
20101130001	417.80	680.30	686.6	0.93	34.83
20101130002	393.80	647.80	653.1	0.82	32.37
20101130003	468.70	725.80	711.4	-1.98	16.55
20102230004	453.10	686.50	665.7	-3.03	33.86

Test no.	$T_{sn,final}$ *(K)*	ΔT *(K)*	$H_{cal,\ tot}$ *(J)*	H_{Sn} *(J)*	*% diff*
20101118004	366.20	14.60	3753	3730	0.62
20101119001	314.40	19.20	4664	4691	-0.58
20101119002	329.00	17.30	4303	4340	-0.85
20101119003	353.00	20.70	5267	5236	0.59
20101119004	344.70	8.00	2048	2066	-0.87
20101130001	433.10	15.30	4256	4208	1.14
20101130002	408.40	14.60	3896	3855	1.06
20101130003	475.40	6.70	1943	2000	-2.85
20102230004	466.20	13.10	3687	3854	-4.33

Appendix E: Summary of Properties

The following tables provide a summary of the thermophysical properties that were collected for this study. In most cases there was insufficient data for W_2C because it is only stable at elevated temperatures; therefore, it was assumed that the properties of W_2C closely match those of WC.

Table E.1 Temperature dependant density, heat capacity and enthalpy for Ni and WC.

Ni [26]				*WC [56-58]*			
T (K)	ρ (kg/m^3)	c_p (J/m^{3}K)	H (J/m^3)	T (K)	ρ (kg/m^3)	c_p (J/m^{3}K)	H (J/m^3)
298	8900	3.791E+06	0	298	15692	2.944E+06	0
373	8865	4.255E+06	3.014E+08	300	15692	2.949E+06	5.368E+06
473	8819	4.824E+06	7.496E+08	400	15666	3.180E+06	3.138E+08
573	8772	6.175E+06	1.307E+09	500	15641	3.360E+06	6.510E+08
673	8726	4.677E+06	1.702E+09	600	15616	3.506E+06	1.007E+09
773	8680	4.644E+06	2.161E+09	700	15591	3.630E+06	1.376E+09
873	8634	4.662E+06	2.607E+09	800	15566	3.737E+06	1.758E+09
973	8588	4.784E+06	3.066E+09	900	15541	3.832E+06	2.150E+09
1073	8542	4.903E+06	3.536E+09	1000	15516	3.917E+06	2.552E+09
1173	8495	5.012E+06	4.010E+09	1100	15491	3.993E+06	2.963E+09
1273	8449	5.112E+06	4.495E+09	1200	15465	4.063E+06	3.383E+09
1373	8402	5.134E+06	4.982E+09	1240	15455	4.090E+06	3.553E+09
1473	8356	5.156E+06	5.465E+09	1276	15446	4.113E+06	3.620E+09
1573	8310	5.127E+06	5.950E+09	1391	15417	4.182E+06	4.118E+09
1673	8264	5.099E+06	6.429E+09	1499	15390	4.242E+06	4.494E+09
1728	8238	5.083E+06	6.689E+09	1600	15365	4.295E+06	4.902E+09
1728	7850	5.762E+06	8.706E+09	1710	15337	4.348E+06	5.412E+09
1773	7796	5.722E+06	8.903E+09	1819	15310	4.398E+06	5.815E+09
1873	7676	5.634E+06	9.326E+09	1912	15287	4.438E+06	6.300E+09

Table E.2 Temperature dependant density, heat capacity and enthalpy for the Ni/WC tubular wire. Above the melting temperature of pure Ni it is assumed that there is no mixing between the Ni and WC/W_2C powder.

Wire		
T (K)	c_p (J/m^3K)	H (J/m^3)
298	2.412E+06	0
373	2.638E+06	1.651E+08
473	2.910E+06	4.599E+08
573	3.464E+06	7.977E+08
673	2.955E+06	1.070E+09
773	2.983E+06	1.369E+09
873	3.026E+06	1.663E+09
973	3.103E+06	1.962E+09
1073	3.175E+06	2.265E+09
1173	3.240E+06	2.569E+09
1273	3.297E+06	2.878E+09
1373	3.322E+06	3.187E+09
1473	3.344E+06	3.494E+09
1573	3.344E+06	3.803E+09
1673	3.340E+06	4.109E+09
1728	3.337E+06	4.276E+09
1728	3.588E+06	5.022E+09
1773	3.575E+06	5.154E+09
1873	3.543E+06	5.439E+09

Table E.3 Effective thermal conductivity and electrical resistivity for Ni and WC/W$_2$C powder.

Ni[26]			*WC[59]*		
T (K)	λ (W/mK)	ρ_r (Ωm)	T (K)	λ (W/mK)	ρ_r (Ωm)
298	90	8.096E-08	298	0.098	7.428E-05
373	87	1.048E-07	373	0.096	9.468E-05
473	76	1.522E-07	473	0.095	1.215E-04
573	64	2.189E-07	573	0.096	1.467E-04
673	60	2.742E-07	673	0.097	1.692E-04
773	62	3.048E-07	773	0.100	1.883E-04
873	65	3.284E-07	873	0.105	2.034E-04
973	67	3.551E-07	973	0.111	2.145E-04
1073	71	3.695E-07	1073	0.118	2.218E-04
1173	72.7	3.945E-07	1173	0.127	2.256E-04
1273	76.7	4.058E-07	1273	0.137	2.266E-04
1373	79.5	4.223E-07	1373	0.149	2.254E-04
1473	82	4.392E-07	1473	0.162	2.223E-04
1573	83.5	4.606E-07	1573	0.176	2.179E-04
1673	85	4.812E-07	1673	0.192	2.126E-04
1728	86.5	4.884E-07	1728	0.202	2.094E-04
1728	69	6.123E-07	1728	0.202	2.094E-04
1773	69	6.283E-07	1773	0.210	2.067E-04
1873	69	6.637E-07	1873	0.228	2.005E-04

Table E.4 Effective thermal conductivity and electrical resistivity for the tubular wire. Calculated electrical resistivity is compared to the measured values below

Wire				
T (K)	λ (W/mK)	ρ_r (Ωm) (Calc.)	T (K) (Measured)	ρ_r (Ωm) (Measured)
298	33.5	2.186E-07	295.2	1.778E-07
373	32.4	2.830E-07	324.3	2.051E-07
473	28.4	4.108E-07	393.3	2.663E-07
573	23.9	5.908E-07	437.5	3.115E-07
673	22.5	7.400E-07	480	3.665E-07
773	23.2	8.226E-07	532	4.278E-07
873	24.4	8.861E-07	608	5.368E-07
973	25.1	9.581E-07	630	5.801E-07
1073	26.6	9.970E-07	686	6.592E-07
1173	27.3	1.064E-06	721	6.960E-07
1273	28.8	1.095E-06	774	7.423E-07
1373	29.8	1.139E-06	824	7.810E-07
1473	30.8	1.185E-06	875	8.138E-07
1573	31.4	1.242E-06	927	8.453E-07
1673	31.9	1.298E-06	967	8.698E-07
1728	32.5	1.317E-06	1029	8.981E-07
1728	26.0	1.650E-06	1073	9.267E-07
1773	26.0	1.693E-06	1122	9.574E-07
1873	26.1	1.788E-06	1171	9.864E-07
			1221	1.019E-06
			1270	1.055E-06
			1319	1.096E-06
			1365	1.137E-06
			1383	1.157E-06

Appendix F: Matlab Code

```
% This code allows for the calculation of the calorimeter
interpolation
% functions. The c values are geometry specific, therefore if the
locations
% of the thermocouples change they will have to be recalculated.

% calibration functions for each calorimeter

% linear correction function for thermocouples
% TC1 1.00038716178387E+00x - 2.23525911530366E-01
% TC2 1.00383572388361E+00x - 1.03302524712160E+00
% TC3 9.99585975261211E-01x - 1.97629437159787E-01
% TC4 1.00107320973242E+00x - 5.64381709063400E-01
% TC5 1.00383556974132E+00x - 1.06641745924072E+00
% TC6 1.00458209384896E+00x - 1.24979968333064E+00
% TC7 1.00383294932949E+00x - 9.98322628326948E-01
% TC8 1.00210697060091E+00x - 6.60308566463250E-01
% TC9 1.00009937361094E+00x + 2.21390078312539E-02
% TC10 9.99815037359825E-01x + 3.29002553268273E-02

% ****BEGIN COPY HERE****

% import data from text file. Change directory to call the file
of
% interest.
Data=load('C:\Documents and
Settings\kevin\Desktop\Masters\Temperature\ASCII\ASCII\2011010500
7_steel_matlab.txt');
time=(0:0.1:(length(Data)-1)*0.1)';

% converging all thermocouples to the average at the start of the
test.
% This is saying the the calorimeter is initially isothermal.
T1in= 1.00038716178387E+00*Data(1,1) - 2.23525911530366E-01;
T2in= 1.00383572388361E+00*Data(1,2) - 1.03302524712160E+00;
T3in= 9.99585975261211E-01*Data(1,3) - 1.97629437159787E-01;
T4in= 1.00107320973242E+00*Data(1,4) - 5.64381709063400E-01;
T5in= 1.00383556974132E+00*Data(1,5) - 1.06641745924072E+00;
T6in= 1.00458209384896E+00*Data(1,6) - 1.24979968333064E+00;
T7in= 1.00383294932949E+00*Data(1,7) - 9.98322628326948E-01;
T8in= 1.00210697060091E+00*Data(1,8) - 6.60308566463250E-01;
T9in= 1.00009937361094E+00*Data(1,15) + 2.21390078312539E-02;
T10in= 9.99815037359825E-01*Data(1,16) + 3.29002553268273E-02;

% average temperature from the first data point collected. avgT
is the
% initial temperature of the calorimeter
avgT=(T1in+T2in+T3in+T4in+T5in+T6in+T7in+T8in+T9in+T10in)/10;
```

```
% find tdiff using the corrected TC values.
T1diff=T1in-avgT;
T2diff=T2in-avgT;
T3diff=T3in-avgT;
T4diff=T4in-avgT;
T5diff=T5in-avgT;
T6diff=T6in-avgT;
T7diff=T7in-avgT;
T8diff=T8in-avgT;
T9diff=T9in-avgT;
T10diff=T10in-avgT;

% if/then for linear correction function
if T1diff <0 TC1corrected=(1.00038716178387E+00*Data(1:end,1) -
2.23525911530366E-01)+abs(T1diff); end
if T1diff >0 TC1corrected=(1.00038716178387E+00*Data(1:end,1) -
2.23525911530366E-01)-abs(T1diff); end
if T2diff <0 TC2corrected=(1.00383572388361E+00*Data(1:end,2) -
1.03302524712160E+00)+abs(T2diff); end
if T2diff >0 TC2corrected=(1.00383572388361E+00*Data(1:end,2) -
1.03302524712160E+00)-abs(T2diff); end
if T3diff <0 TC3corrected=(9.99585975261211E-01*Data(1:end,3) -
1.97629437159787E-01)+abs(T3diff); end
if T3diff >0 TC3corrected=(9.99585975261211E-01*Data(1:end,3) -
1.97629437159787E-01)-abs(T3diff); end
if T4diff <0 TC4corrected=(1.00107320973242E+00*Data(1:end,4) -
5.64381709063400E-01)+abs(T4diff); end
if T4diff >0 TC4corrected=(1.00107320973242E+00*Data(1:end,4) -
5.64381709063400E-01)-abs(T4diff); end
if T5diff <0 TC5corrected=(1.00383556974132E+00*Data(1:end,5) -
1.06641745924072E+00)+abs(T5diff); end
if T5diff >0 TC5corrected=(1.00383556974132E+00*Data(1:end,5) -
1.06641745924072E+00)-abs(T5diff); end
if T6diff <0 TC6corrected=(1.00458209384896E+00*Data(1:end,6) -
1.24979968333064E+00)+abs(T6diff); end
if T6diff >0 TC6corrected=(1.00458209384896E+00*Data(1:end,6) -
1.24979968333064E+00)-abs(T6diff); end
if T7diff <0 TC7corrected=(1.00383294932949E+00*Data(1:end,7) -
9.98322628326948E-01)+abs(T7diff); end
if T7diff >0 TC7corrected=(1.00383294932949E+00*Data(1:end,7) -
9.98322628326948E-01)-abs(T7diff); end
if T8diff <0 TC8corrected=(1.00210697060091E+00*Data(1:end,8) -
6.60308566463250E-01)+abs(T8diff); end
if T8diff >0 TC8corrected=(1.00210697060091E+00*Data(1:end,8) -
6.60308566463250E-01)-abs(T8diff); end
if T9diff <0 TC9corrected=(1.00009937361094E+00*Data(1:end,15) +
2.21390078312539E-02)+abs(T9diff); end
if T9diff >0 TC9corrected=(1.00009937361094E+00*Data(1:end,15) +
2.21390078312539E-02)-abs(T9diff); end
if T10diff <0 TC10corrected=(9.99815037359825E-01*Data(1:end,16)
+ 3.29002553268273E-02)+abs(T10diff); end
if T10diff >0 TC10corrected=(9.99815037359825E-01*Data(1:end,16)
+ 3.29002553268273E-02)-abs(T10diff); end

% plot corrected temperatures vs. time
figure1 = figure('Color',[1 1 1]);
```

```
axes1 =
axes('Parent',figure1,'LineWidth',1.25,'FontSize',10,'FontName','
Helvetica Narrow');
box(axes1,'on');
hold(axes1,'all');
plot(time,TC1corrected)
% time,TC2corrected, time,TC3corrected, time,TC4corrected,
time,TC5corrected, time,TC6corrected, time,TC7corrected,
time,TC8corrected, time,TC9corrected, time,TC10corrected)
xlabel('Time (s)','FontSize',12,'FontName','Helvetica Narrow')
ylabel('Temperature (K)','FontSize',12,'FontName','Helvetica
Narrow')


% final temperature of the calorimeter is aken to be the average
of the
% three surface thermocouples
TC2max=max(TC2corrected);
TC5max=max(TC5corrected);
TC8max=max(TC8corrected);
Tf=(TC2max+TC5max+TC8max)/3

% apply interpolation functions to obtain total enthalpy
% c2, c3, c5, c6, c7 are all zero according to the volume
integrals of the
% cylindrical calorimeter. all units are si and are calculated in
the excel
% spreadsheet "Crucible Temp". if numbers on the spreadsheet
change, the
% numbers in this code will change.
% m=mass, v=volume, r=radius, h=height
mcal=0.62296;
vcal=mcal/8930;
rcal=0.02535;
hcal=0.0331;

c1coeff=vcal;
c4coeff=(2*pi*hcal^2*rcal^2)/4;
c8coeff=(pi*hcal*rcal^4)/4;
c9coeff=(pi*hcal*rcal^4)/4;
c10coeff=(2*pi*hcal^3*rcal^2)/6;

% TC1 c values
c1TC1=0.888415841;
c4TC1=28.69415297;
c8TC1=-1893.321718;
c9TC1=-1882.532747;
c10TC1=-1275.309447;

% TC2 c values
c1TC2=0.06832373;
c4TC2=-17.37485823;
c8TC2=210.1882822;
c9TC2=-210.3273411;
c10TC2=769.7511487;
```

```
% TC3 c values
c1TC3=-0.581874393;
c4TC3=55.99537956;
c8TC3=914.0922186;
c9TC3=348.0845307;
c10TC3=-1299.737958;

% TC4 c values
c1TC4=0.550649727;
c4TC4=-48.17302694;
c8TC4=-414.6806391;
c9TC4=411.7798253;
c10TC4=954.7044722;

% TC5 c values
c1TC5=0.067165;
c4TC5=-17.30269254;
c8TC5=-578.5838209;
c9TC5=575.5871607;
c10TC5=769.4110022;

% TC6 c values
c1TC6=-0.578737617;
c4TC6=55.71974856;
c8TC6=1206.286075;
c9TC6=53.94151056;
c10TC6=-1294.230148;

% TC7 c values
c1TC7=0.548956602;
c4TC7=-47.99974403;
c8TC7=-9.718787323;
c9TC7=10.82680443;
c10TC7=950.3311622;

% TC8 c values
c1TC8=0.066124173;
c4TC8=-17.1657672;
c8TC8=368.3955387;
c9TC8=-365.2598196;
c10TC8=764.9853145;

% TC9 c values
c1TC9=-0.579416735;
c4TC9=55.71975117;
c8TC9=-227.0565751;
c9TC9=1480.506706;
c10TC9=-1292.012769;

% TC10 c values
c1TC10=0.550393671;
c4TC10=-48.11294332;
c8TC10=424.3994264;
c9TC10=-422.6066297;
```

```
c10TC10=952.1072227;

% temperature to enthalpy for each tc
% enthalpy vs T for copper (J/kg) AVERAGE OF ALL SOURCES w/o
MILLS TO 800K
HcuTC1=3.996237E+02*TC1corrected - 1.191949E+05;
HcuTC2=3.996237E+02*TC2corrected - 1.191949E+05;
HcuTC3=3.996237E+02*TC3corrected - 1.191949E+05;
HcuTC4=3.996237E+02*TC4corrected - 1.191949E+05;
HcuTC5=3.996237E+02*TC5corrected - 1.191949E+05;
HcuTC6=3.996237E+02*TC6corrected - 1.191949E+05;
HcuTC7=3.996237E+02*TC7corrected - 1.191949E+05;
HcuTC8=3.996237E+02*TC8corrected - 1.191949E+05;
HcuTC9=3.996237E+02*TC9corrected - 1.191949E+05;
HcuTC10=3.996237E+02*TC10corrected - 1.191949E+05;

% enthalpy vs T for copper (J/kg) Mills interpolated to 800K
% HcuTC1=4.13290735E+02*TC1corrected - 1.24873099E+05;
% HcuTC2=4.13290735E+02*TC2corrected - 1.24873099E+05;
% HcuTC3=4.13290735E+02*TC3corrected - 1.24873099E+05;
% HcuTC4=4.13290735E+02*TC4corrected - 1.24873099E+05;
% HcuTC5=4.13290735E+02*TC5corrected - 1.24873099E+05;
% HcuTC6=4.13290735E+02*TC6corrected - 1.24873099E+05;
% HcuTC7=4.13290735E+02*TC7corrected - 1.24873099E+05;
% HcuTC8=4.13290735E+02*TC8corrected - 1.24873099E+05;
% HcuTC9=4.13290735E+02*TC9corrected - 1.24873099E+05;
% HcuTC10=4.13290735E+02*TC10corrected - 1.24873099E+05;

% enthalpy vs T for copper (J/kg) White interpolated to 450K
% HcuTC1=3.921148E+02*TC1corrected - 1.170866E+05;
% HcuTC2=3.921148E+02*TC2corrected - 1.170866E+05;
% HcuTC3=3.921148E+02*TC3corrected - 1.170866E+05;
% HcuTC4=3.921148E+02*TC4corrected - 1.170866E+05;
% HcuTC5=3.921148E+02*TC5corrected - 1.170866E+05;
% HcuTC6=3.921148E+02*TC6corrected - 1.170866E+05;
% HcuTC7=3.921148E+02*TC7corrected - 1.170866E+05;
% HcuTC8=3.921148E+02*TC8corrected - 1.170866E+05;
% HcuTC9=3.921148E+02*TC9corrected - 1.170866E+05;
% HcuTC10=3.921148E+02*TC10corrected - 1.170866E+05;

% enthalpy vs T for copper (J/kg) Thermocalc interpolated to 450K
% HcuTC1=4.360650E+02*TC1corrected - 1.299474E+05;
% HcuTC2=4.360650E+02*TC2corrected - 1.299474E+05;
% HcuTC3=4.360650E+02*TC3corrected - 1.299474E+05;
% HcuTC4=4.360650E+02*TC4corrected - 1.299474E+05;
% HcuTC5=4.360650E+02*TC5corrected - 1.299474E+05;
% HcuTC6=4.360650E+02*TC6corrected - 1.299474E+05;
% HcuTC7=4.360650E+02*TC7corrected - 1.299474E+05;
% HcuTC8=4.360650E+02*TC8corrected - 1.299474E+05;
% HcuTC9=4.360650E+02*TC9corrected - 1.299474E+05;
% HcuTC10=4.360650E+02*TC10corrected - 1.299474E+05;

% enthalpy vs T for copper (J/kg) Stephens interpolated to 450K
% HcuTC1=3.759583E+02*TC1corrected - 1.120356E+05;
% HcuTC2=3.759583E+02*TC2corrected - 1.120356E+05;
% HcuTC3=3.759583E+02*TC3corrected - 1.120356E+05;
```

```
% HcuTC4=3.759583E+02*TC4corrected - 1.120356E+05;
% HcuTC5=3.759583E+02*TC5corrected - 1.120356E+05;
% HcuTC6=3.759583E+02*TC6corrected - 1.120356E+05;
% HcuTC7=3.759583E+02*TC7corrected - 1.120356E+05;
% HcuTC8=3.759583E+02*TC8corrected - 1.120356E+05;
% HcuTC9=3.759583E+02*TC9corrected - 1.120356E+05;
% HcuTC10=3.759583E+02*TC10corrected - 1.120356E+05;

% enthalpy vs T for copper (J/kg) Mills interpolated to 450K
% HcuTC1=3.945946E+02*TC1corrected - 1.178054E+05;
% HcuTC2=3.945946E+02*TC2corrected - 1.178054E+05;
% HcuTC3=3.945946E+02*TC3corrected - 1.178054E+05;
% HcuTC4=3.945946E+02*TC4corrected - 1.178054E+05;
% HcuTC5=3.945946E+02*TC5corrected - 1.178054E+05;
% HcuTC6=3.945946E+02*TC6corrected - 1.178054E+05;
% HcuTC7=3.945946E+02*TC7corrected - 1.178054E+05;
% HcuTC8=3.945946E+02*TC8corrected - 1.178054E+05;
% HcuTC9=3.945946E+02*TC9corrected - 1.178054E+05;
% HcuTC10=3.945946E+02*TC10corrected - 1.178054E+05;

% v- interpolation function for each thermocouple. integrated
form of hi,
% units are m^3
v1=c1coeff*c1TC1+c4coeff*c4TC1+c8coeff*c8TC1+c9coeff*c9TC1+c10coe
ff*c10TC1;
v2=c1coeff*c1TC2+c4coeff*c4TC2+c8coeff*c8TC2+c9coeff*c9TC2+c10coe
ff*c10TC2;
v3=c1coeff*c1TC3+c4coeff*c4TC3+c8coeff*c8TC3+c9coeff*c9TC3+c10coe
ff*c10TC3;
v4=c1coeff*c1TC4+c4coeff*c4TC4+c8coeff*c8TC4+c9coeff*c9TC4+c10coe
ff*c10TC4;
v5=c1coeff*c1TC5+c4coeff*c4TC5+c8coeff*c8TC5+c9coeff*c9TC5+c10coe
ff*c10TC5;
v6=c1coeff*c1TC6+c4coeff*c4TC6+c8coeff*c8TC6+c9coeff*c9TC6+c10coe
ff*c10TC6;
v7=c1coeff*c1TC7+c4coeff*c4TC7+c8coeff*c8TC7+c9coeff*c9TC7+c10coe
ff*c10TC7;
v8=c1coeff*c1TC8+c4coeff*c4TC8+c8coeff*c8TC8+c9coeff*c9TC8+c10coe
ff*c10TC8;
v9=c1coeff*c1TC9+c4coeff*c4TC9+c8coeff*c8TC9+c9coeff*c9TC9+c10coe
ff*c10TC9;
v10=c1coeff*c1TC10+c4coeff*c4TC10+c8coeff*c8TC10+c9coeff*c9TC10+c
10coeff*c10TC10;

% total calorimeter enthalpy- sum of interpolation function
multiplied by
% thermocouple measurements converted to enthalpy
% units are J
Htot=8930*(HcuTC1*v1+HcuTC2*v2+HcuTC3*v3+HcuTC4*v4+HcuTC5*v5+HcuT
C6*v6+HcuTC7*v7+HcuTC8*v8+HcuTC9*v9+HcuTC10*v10);
Hcal=(max(Htot)-min(Htot));

% calibration function
calib=0.1046*(Tf-298);

% overall enthalpy
```

```
Hcaltot=Hcal-Hcal*(3.5992/100)+Hcal*(calib/100)

% plot of total enthalpy vs. time
figure2 = figure('Color',[1 1 1]);
axes1 =
axes('Parent',figure2,'LineWidth',1.25,'FontSize',12,'FontName','
Time New Roman');
box(axes1,'on');
hold(axes1,'all');
plot(time,Htot)
xlabel('Time (s)','FontSize',12,'FontName','Times New Roman');
ylabel('Enthalpy (J)','FontSize',12,'FontName','Times New
Roman');

% enthalpy as a function of z and time.
% H(o,o,z,t)=sum(hi(o,o,z,t)*Hi)
% this is looking at how enthalpy changes along the z axis while
time is
% changing. the non-integrated form is used because we are
looking at
% profiles, not at overall enthalpy of the volume. hi's are
dimensionless,
% HcuTCi is in J/kg.
% z=(0:(hcal/49):hcal)';
% h1=(c1TC1+c4TC1*z+c10TC1*z.^2)';
% h2=(c1TC2+c4TC2*z+c10TC2*z.^2)';
% h3=(c1TC3+c4TC3*z+c10TC3*z.^2)';
% h4=(c1TC4+c4TC4*z+c10TC4*z.^2)';
% h5=(c1TC5+c4TC5*z+c10TC5*z.^2)';
% h6=(c1TC6+c4TC6*z+c10TC6*z.^2)';
% h7=(c1TC7+c4TC7*z+c10TC7*z.^2)';
% h8=(c1TC8+c4TC8*z+c10TC8*z.^2)';
% h9=(c1TC9+c4TC9*z+c10TC9*z.^2)';
% h10=(c1TC10+c4TC10*z+c10TC10*z.^2)';

% H at 18.7 seconds
%
H1=mcal*(h1*HcuTC1(187,1)+h2*HcuTC2(187,1)+h3*HcuTC3(187,1)+h4*Hc
uTC4(187,1)+h5*HcuTC5(187,1)+h6*HcuTC6(187,1)+h7*HcuTC7(191,1)+h8
*HcuTC8(187,1)+h9*HcuTC9(187,1)+h10*HcuTC10(187,1));
% H at 19.1 seconds for diferent z depths specified above
%
H2=mcal*(h1*HcuTC1(191,1)+h2*HcuTC2(191,1)+h3*HcuTC3(191,1)+h4*Hc
uTC4(191,1)+h5*HcuTC5(191,1)+h6*HcuTC6(191,1)+h7*HcuTC7(191,1)+h8
*HcuTC8(191,1)+h9*HcuTC9(191,1)+h10*HcuTC10(191,1));
% H at 19.5 seconds
%
H3=mcal*(h1*HcuTC1(195,1)+h2*HcuTC2(195,1)+h3*HcuTC3(195,1)+h4*Hc
uTC4(195,1)+h5*HcuTC5(195,1)+h6*HcuTC6(195,1)+h7*HcuTC7(195,1)+h8
*HcuTC8(195,1)+h9*HcuTC9(195,1)+h10*HcuTC10(195,1));
% H at 26.6 seconds
%
H4=mcal*(h1*HcuTC1(266,1)+h2*HcuTC2(266,1)+h3*HcuTC3(266,1)+h4*Hc
uTC4(266,1)+h5*HcuTC5(266,1)+h6*HcuTC6(266,1)+h7*HcuTC7(266,1)+h8
*HcuTC8(266,1)+h9*HcuTC9(266,1)+h10*HcuTC10(266,1));
% H at 36.5 seconds
```

```
%
H5=mcal*(h1*HcuTC1(365,1)+h2*HcuTC2(365,1)+h3*HcuTC3(365,1)+h4*Hc
uTC4(365,1)+h5*HcuTC5(365,1)+h6*HcuTC6(365,1)+h7*HcuTC7(365,1)+h8
*HcuTC8(365,1)+h9*HcuTC9(365,1)+h10*HcuTC10(365,1));
% H at 61.3 seconds
%
H6=mcal*(h1*HcuTC1(613,1)+h2*HcuTC2(613,1)+h3*HcuTC3(613,1)+h4*Hc
uTC4(613,1)+h5*HcuTC5(613,1)+h6*HcuTC6(613,1)+h7*HcuTC7(613,1)+h8
*HcuTC8(613,1)+h9*HcuTC9(613,1)+h10*HcuTC10(613,1));

% plotting H vs. depth for  different times
% figure3 = figure('Color',[1 1 1]);
% axes1 = axes('Parent',figure3,'XDir','reverse');
% xlim(axes1,[0 0.0331]);
% box(axes1,'on');
% hold(axes1,'all');
% plot(z,H1,z,H2,z,H3,z,H4,z,H5,z,H6);
% xlabel('Surface to Bottom of Cal. (m)');
% ylabel('Enthalpy (J)');



% These lines were used to calculate initial temperatures based
on the
% calorimeter enthalpy and the thermophysical properites of the
electrode
% material. Caution should be used when calculating for the Ni/WC
wires as
% the enthalpy balance changes if some WC dissolves.

% FOR Castolin NiWC:

% melting point of nickel (K)
% Tmnickel=1728;
% Mdep=7.36;

% enthaply functions. all are functions of temperature and have
constants
% that have been omitted because they will cancel. All T's are in
K.
% fractions are weight percent.

% solid wire
% H= 0.40096061*T - 130.37432249

% liquid wire
%  H=0.48647515*T - 118.40023369
% A = 0.48647515;
%
% Hsolid = 0.40096061*(Tmnickel-Tf);
% Hfus = 159;
% Hliq = (Hcaltot/Mdep)-Hfus-Hsolid;
%
% Ti=(Hliq/A)+ Tmnickel
```

```
% CTC Wire:

% melting point of nickel (K)
% Tmnickel=1676;
% Mdep=5.43;

% enthaply functions. all are functions of temperature and have
constants
% that have been omitted because they will cancel. All T's are in
K.
% fractions are weight percent.

% solid wire
% H= 0.3554*T - 120.869
% B = 0.3554;
% liquid wire
% H=0.6419*T - 402.11
% A = 0.6419;
%
% Hsolid = B*(Tmnickel-Tf);
% Hfus = 181.3;
% Hliq = (Hcaltot/Mdep)-Hfus-Hsolid;
%
% Ti=(Hliq/A)+ Tmnickel



% FOR TIN CALIBRATION:

% enthalpy of fusion (J/g), melting temp (K), and mass (g) of Sn:
% Hfussn=60.61;
% Tfussn=505.12;
% msn=33.86;

% Initial Sn temp (K). TC9 is channel 18, column 19. TC10 is
channel 19 column 20:
% sn1TC9=1.004937083806E+00*Data(1:end,17) + 1.409474177953E-01;
% sn2TC10= 1.009807897595E+00*Data(1:end,18) - 1.006894429918E-
01;
% avgTsn=(sn1TC9+sn2TC10)/2;
% Tsnin=max(avgTsn);



% Final Sn temp (K)
% Tsnfin=(TC2max+TC5max+TC8max)/3;

% solid enthalpy funcion (J/g):
% H = 0.000080*T^2 + 0.180125*T - 7.531335

% liquid enthalpy function (J/g):
% H = 0.238060*T + 44.622550

% A=0.00008;
% B=0.180125;
% D=0.238060;
```

```
% Sn enthalpy (J):
% Hsn=(0.238060*(Tsnin-Tfussn) + Hfussn + ((0.000080*Tfussn^2 +
0.180125*Tfussn)-(0.000080*Tsnfin^2 +0.180125*Tsnfin)))*msn

% Initial temp of tin based on calorimeter enthalpy:
% Tsnfromcal=((-A*Tfussn^2-B*Tfussn+A*Tsnfin^2+B*Tsnfin-
Hfussn)/D)+(Hcaltot/(msn*D))+Tfussn

% FOR STEEL TRIALS:
% enthalpy functions for pure iron in J/g. constant will cancel
so they are
% disregarded

% Transition temperatures (K)
% Tfus=1811;
% Talphagamma=1184;

% Ferrite
% H = 0.0003x2 + 0.2029x - 86.244
% A=0.00032194;
% B=0.20289;
% dHferrite=A*(Talphagamma^2-Tf^2)+B*(Talphagamma-Tf);

% gamma/delta
% H = 0.6893x - 208.17
% D=0.689253;
% dHgammadelta=D*(Tfus-Talphagamma);

% liquid
% H = 0.8302x - 205.77
% F=0.830154;

% fusion (J/g)
% Hfus=247;

% Mass of deposition (g)
% mfe=11.4;

% initial droplet temperature
% Ti=((Hcaltot/(F*mfe))-(A*(Talphagamma^2-Tf^2)+B*(Talphagamma-
Tf)-D*(Tfus-Talphagamma)-Hfus)/F)+Tfus;
% dHliq=(Hcaltot/mfe)-dHferrite-dHgammadelta-Hfus;
%
% Ti=(dHliq/F)+Tfus

% ****END OF CODE****
```